Quantifying uncertainty in nanofiltration transport models for enhanced metals recovery

Quantifying uncertainty in nanofiltration transport models for enhanced metals recovery

Danyal Rehman[a,b], Fareed Sheriff[a], John H. Lienhard[a,*]

[a]*Rohsenow Kendall Heat Transfer Laboratory, Massachusetts Institute of Technology, Cambridge, MA 02139-4307, U.S.A*
[b]*Center for Computational Science and Engineering, Massachusetts Institute of Technology, Cambridge, MA 02139-4307, U.S.A*

Abstract

To decarbonize our global energy system, sustainably harvesting metals from diverse sourcewaters is essential. Membrane-based processes have recently shown great promise in meeting these needs by achieving high metal ion selectivities with relatively low water and energy use. An example is nanofiltration, which harnesses steric, dielectric, and Donnan exclusion mechanisms to perform size- and charge-based fractionation of metal ions. To further optimize nanofiltration systems, multicomponent models are needed; however, conventional methods necessitate large amounts of data for model calibration, introduce substantial uncertainty into the characterization process, and often yield poor results when extrapolated. In this work, we develop a new computational architecture to alleviate these concerns. Specifically, we develop a framework that: (**1**) reduces the data requirement for model calibration to only charged species measurements; (**2**) eliminates uncertainty propagation problems present in conventional characterization processes; (**3**) enables exploration of pH optimization for enhancing metal ion selectivities; and (**4**) enables uncertainty quantification to assess the sensitivity of partition coefficients and ion driving forces to pore size distributions. Our framework captures eight independent datasets comprising over 500 measurements to within $\pm 15\%$. Our studies also suggest that the expectation-maximization algorithm can effectively learn pore size distributions and that optimizing pH can improve metal ion selectivities by a factor of 3–10$\times$. Our findings also reveal that image charges appear to play a less pronounced role in dielectric exclusion under the studied conditions and that ion driving forces are more sensitive to pore size distributions than partition coefficients.

Keywords: ion selectivity, metal recovery, transport models, metaheuristics, bilevel optimization, nanofiltration

Number of pages: 22. Number of figures: 9. Number of tables: 0.

Graphical Abstract

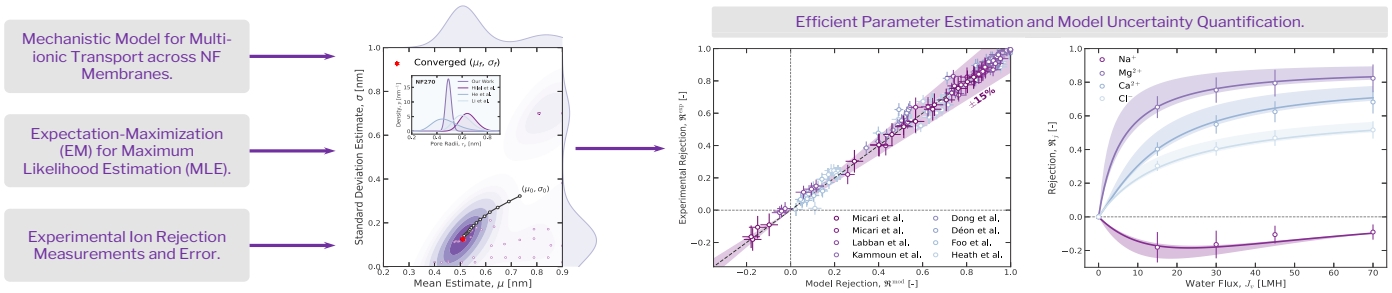

*Corresponding author.
Email address: lienhard@mit.edu

1. Introduction and Background

Sustainably harvesting valuable metals is essential to easing our clean energy transition and combatting climate change (Sadoff et al., 2020; DuChanois et al., 2022). To decarbonize the global energy system by 2050, nearly 3 billion tonnes of metals are needed, based on current estimates by the World Bank (Sovacool et al., 2020). Owing to the rapid growth of the electric vehicle (EV) industry, the demand for lithium is expected to double by 2025 and quadruple by 2030. This increased global demand has the potential to induce significant supply risks, if sustainable methods to harvest metals are not further developed for industrial operation. A relatively untapped and promising source of these elements is the ocean: an enormous reservoir of industrially valuable resources. Certain metals, like lithium and magnesium, are orders of magnitude more abundant in seawater than on land (Ivanov et al., 2017; DuChanois et al., 2023).

Membrane-based separations processes have shown great promise in treating diverse saline sourcewaters and achieving high metal ion selectivities (Kulkarni, 2003; Kurniawan et al., 2006; Razmjou et al., 2019; Roobavannan et al., 2020; Arana Juve et al., 2022; Ahdab et al., 2021). These processes often exploit a combination of steric, dielectric, and Donnan exclusion mechanisms to achieve size- and charge-based separation (Epsztein et al., 2015, 2020). Nanofiltration (NF), a relatively well-established separations technique, is a pressure-driven process that exploits these selectivity mechanisms (as illustrated in Fig. 1) for metal recovery, water softening, pharmaceutical separations, and desalination (Schäfer et al., 2005; Rahimpour et al., 2010; Marchetti et al., 2014). To better optimize NF's ion selectivity and performance, accurate mechanistic models are essential (Murthy and Chaudhari, 2009; Hegde et al., 2022).

The first models for solute transport in NF were derived from irreversible thermodynamics in the 1960s (Kedem and Katchalsky, 1963; Spiegler and Kedem, 1966). These phenomenological models treated the membranes as a black box, which intrinsically neglected the relationship between selective performance and membrane structural/electrical properties. Consequently, these models interpolated well but struggled to generalize performance outside the regressed operating range (Perry and Linder, 1989). In the mid-1990s, Bowen and Mukhtar developed the Donnan Steric Pore Model (DSPM), which combined the extended Nernst-Planck partial differential equations with hindered transport relations in the membrane pores to establish an explicit relationship between membrane parameters and selective performance (Deen, 1987; Bowen and Mukhtar, 1996; Bowen and Mohammad, 1998). DSPM, however, failed to account for a fundamental selectivity mechanism: dielectric exclusion. The model was later augmented to develop the Donnan Steric Pore Model with Dielectric Exclusion (DSPM-DE) (Bowen and Welfoot, 2002a), which combined the original DSPM model with the Born equation to account for ion solvation (Duignan and Zhao, 2020).

Since the development of DSPM-DE, many efforts have been made to mitigate some of the model's underlying simplifications, while improving predictive performance. For example, DSPM-DE most frequently uses an averaged value for pore size, despite measured pore size distributions being more representative of polyamide membrane morphologies (Hilal et al., 2005). Bowen et al. attempted to determine the pore size distributions of various NF membranes using atomic force microscopy (AFM) and integrate these distributions into the governing model (Bowen et al., 1997). This was achieved by prescribing a probability density function of a discrete log-normal distribution to the pore sizes and fitting the model to experimental data (Bowen et al., 1997; Bowen and Welfoot, 2002b). Other groups, including Wang et al., Li et al., and He et al., have all attempted to characterize NF membrane pores using probabilistic distributions (Wang et al., 2014; Li et al., 2019; He et al., 2022). Their findings have strengthened the claims that a log-normal pore size distribution is characteristic of NF membranes; however, the distribution characterization procedure has typically required a substantial number of pure water and single solute experiments.

The efficacy of the Born model in accounting for dielectric exclusion is another contested simplification of DSPM-DE (Wang and Lin, 2021). The Born equation is used to capture ion solvation; however, it frequently overestimates solvation energies, especially for cations (Starov and Churaev, 1993; Szymczyk and Fievet, 2005; Saliha et al., 2009). Since partial dehydration has also been shown to play a significant role in dielectric exclusion (as well as steric exclusion), the ionic radii term present in the Born equation is often modified into the hydrodynamic Stokes radii (Hussain et al., 2007). Numerous authors have investigated the applicability of cavity radii, covalent radii, Born radii, and Pauling radii to varying degrees of success throughout the literature (Hussain et al., 2008). The other often-disregarded component of dielectric exclusion is the presence of fictitious image charges that develop between media of different dielectric constants. Bandini and Vezzani as well as Szymczyk and Fievet tried to incorporate these effects into the DSPM-DE model to fully capture dielectric effects (Szymczyk and Fievet, 2005; Bandini and Vezzani, 2003). The excess solvation energies were calculated from analytical solutions to the cylindrical Poisson equation for point-like charges by Yaroshchuk in slit-like nanopores. These were then used to characterize the repulsive image forces that occur from differences in dielectric constants between the solvent and membrane matrix (Yaroshchuk, 2000, 2001). Although technically more accurate, the mathematical complexities of the approach serve as a barrier to more frequent adoption (Oatley et al., 2012).

Another concern surrounding the DSPM-DE model arises from the tedious membrane characterization procedure (Wang and Lin, 2021). Typically, a large number of experiments is needed to quantify the four governing membrane parameters: (**1**) pore size, r_p; (**2**) effective membrane thickness, Δx_e; (**3**) dielectric constant in the membrane pores, ζ_p; and (**4**) volumetric membrane charge density, χ_d. First, uncharged solute studies are required to quantify the pore radius, r_p, followed by pure water permeability experiments for the effective membrane thickness, Δx_e. Subsequently, the determined parameters are combined with single salt studies at the membrane's isoelectric point (IEP) to quantify the dielectric constant in the membrane pores (assuming that the membrane is uncharged under these operating conditions). Finally, charged species studies are performed to quantify the membrane charge density, χ_d, which is most frequently assumed to be homogeneously distributed across the membrane (although recent studies have shown that it most likely conforms to a heterogenous, composition-dependent structure (Déon et al., 2011; Balannec et al., 2018; Ritt et al., 2020)). The characterization process assumes that the membrane parameters are independent of one another, but evidence in the literature suggests otherwise (Wang and Lin, 2021; Rehman and Lienhard, 2022). In addition to the substantial number of experiments needed for characterization, significant error can also propagate between experiments: Wang and Lin showed that a 10% uncertainty in the dielectric constant can lead to a $\pm$100% uncertainty in membrane charge density (Wang and Lin, 2021). This can result in the regression of unphysical membrane parameters or data that is challenging to

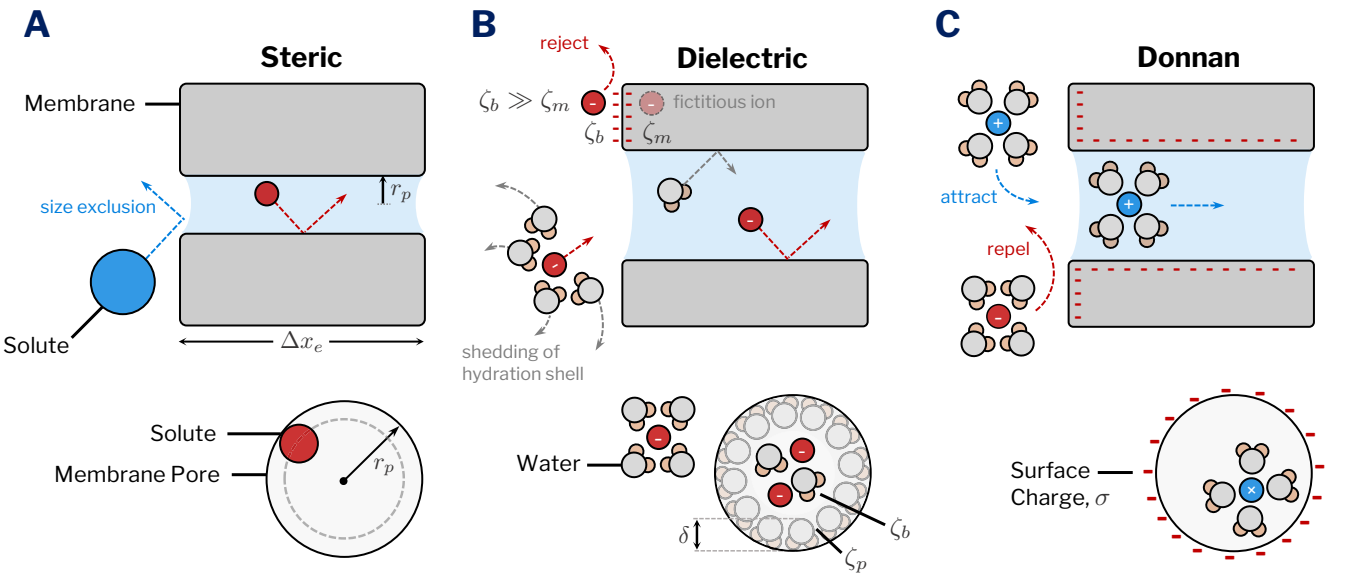

Figure 1: Schematic diagrams of a membrane pore showing exclusion mechanisms. **(A)** Steric rejection fractionates solutes based on their size relative to the pore radius, r_p. **(B)** Dielectric exclusion combines the partial or complete shedding of ion hydration shells before entering the membrane pores with fictitious image forces created at the membrane interface. These image charges are repulsive for both cations and anions, given that the dielectric constant of the solvent, ζ_b, is larger than the dielectric constant of the membrane matrix, ζ_m. The cross section shows a thin film of water molecules with a constrained orientation aggregated near the pore walls, where the dielectric constant of the solvent is reduced to ζ_p. The thickness of the layer of water molecules is denoted by δ. ζ_b and ζ_m were set to 78.54 and 4.5, respectively, in the reported work. **(C)** The Donnan exclusion mechanism fractionates ions based on charge, e.g. negatively-charged ions are repelled by a negatively-charged membrane, whereas positively-charged ions are attracted into the pores. Here, σ is the surface charge of the membrane.

regress (Kammoun et al., 2020; Rehman and Lienhard, 2023).

To reduce the number of underlying simplifications, the authors propose a new computational framework that extends the current DSPM-DE infrastructure. More specifically, the framework aims to achieve the following objectives: (**1**) the introduction of a probabilistic estimation technique to learn pore size distributions from charged species data; (**2**) the consideration of the image charge contribution to the dielectric exclusion mechanism in cylindrical pores; (**3**) the reduction in the number of experiments needed for membrane characterization to *only* charged species data; (**4**) the elimination of assumed relationships between pore size and water flux; (**5**) the removal of the assumption that membrane parameters are independent of one another during characterization; and lastly, (**6**) a quasi Monte Carlo sampling-based uncertainty quantification study and sensitivity analysis to understand the limits of the proposed modelling architecture. The conducted work is validated against eight sets of independent experimental data comprising over 500 multicomponent measurements. The data spans different salinities, compositions, and membrane types to establish the model's predictive capabilities under various operating conditions[1].

[1] All studies performed in this work investigate salinities below that of seawater; studying higher concentrations with the extended Nernst-Planck equations can lead to misleading conclusions because effects of ion complexation and/or inter-species coupling are intrinsically neglected (Foo et al., 2021).

2. Mathematical Model

2.1. Multicomponent Transport in the Selective Layer

The extended Nernst-Planck equations in conjunction with hindered transport theory can describe multicomponent transport in the membrane's selective layer. Using this formulation, the solute mole flux, J_i, can be expressed as:

$$J_i = -D_i K_{i,d} \partial_x C_i + K_{i,c} C_i J_v - \frac{K_{i,d} D_i C_i z_i \mathfrak{F}}{RT} \partial_x \psi, \quad x \in [0, \Delta x_e] \quad (1)$$

Here, $K_{i,c}$ and $K_{i,d}$ are the convective and diffusive hindrance factors for species i, respectively. Both hindrance factors were originally derived from perturbation theory solutions to the Navier-Stokes and are polynomial expressions of λ_i, the ratio of the solutes' Stokes radii, r_i, to the membrane's pore radius, r_p (Deen, 1987; Mavrovouniotis and Brenner, 1988; Ennis et al., 1996). In addition, for species i, D is the bulk diffusion coefficient, z is the ion valence, and C is the concentration. Remaining variables and constants include: J_v, the permeate flux; ψ, the electric potential; T, the absolute temperature; $\mathfrak{F}$, Faraday's constant; and R, the universal gas constant. x is the spatial coordinate orthogonal to the membrane surface. The three terms on the right-hand side of Eq. (1) correspond to the diffusive, convective, and electromigration fluxes of species i, respectively.

2.2. Multicomponent Transport in the Boundary Layer

To account for concentration polarization in the feed-side boundary layer, the extended Nernst-Planck equations are linearized (Geraldes and Afonso, 2007). Under these conditions, the solute flux in the boundary layer is given by the following expression:

$$J_i = -\bar{k}_{c,i} \left[C_{i,f,m} - C_{i,f,b} \right] + J_v C_{i,f,m} - z_i C_{i,f,m} D_i \frac{\mathfrak{F} \xi}{RT} \quad (2)$$

where ξ is the linearized electric potential gradient in the boundary layer. Subscripts f and p denote the feed and permeate, while subscripts b and m denote the bulk fluid and membrane interface, respectively. $\bar{k}_{c,i}$ is a mass transfer coefficient modified to account for membrane permeation (Song et al., 2018). Depending on membrane configuration (hollow-fibre, spiral wound, or coupon-scale), different correlations can be adopted (Labban et al., 2017).

2.3. Equilibrium Partitioning at Solution-Membrane Interface

Although the chemical potential is continuous across the solution-membrane interface, the concentration may not be. This leads to solute partitioning, which affects species rejection and gives rise to ion selectivity (Ahdab et al., 2020; Postel et al., 2016). By equating the chemical potential on both sides of the interface, $\mu_i^{0^-} = \mu_i^{0^+}$, and introducing partition coefficients for steric and dielectric exclusion mechanisms (Geraldes and Afonso, 2007; Giddings et al., 1968), ion fractionation on the feed-side can be expressed as follows:

$$\frac{\gamma_i(0^-)C_{i,f,m}(0^-)}{\gamma_i(0^+)C_{i,f,m}(0^+)} = \phi_{i,\mathrm{S}}\phi_{i,\mathrm{Di}}\phi_{i,\mathrm{Do}} \tag{3}$$

Here, 0^- and 0^+ correspond to the fluid-side and membrane-side in the feed stream, respectively. A reciprocating expression is prescribed to the permeate side. In Eq. (3), $\phi_{i,\mathrm{S}}$ is an ion sieving coefficient, derived from geometric arguments. $\phi_{i,\mathrm{Di}}$ is the dielectric exclusion partition coefficient for species i, and attempts to account for ion solvation and the effects of hydration using the Born model, as well as the effect of image charges from the polarized layer at the membrane-solution interface (Yaroshchuk, 2000, 2001; Dill and Bromberg, 2011). Lastly, $\phi_{i,\mathrm{Do}}$ is the Donnan screening partition coefficient that accounts for the Donnan potential that forms across the membrane under equilibrium conditions (Donnan, 1995).

The steric partition coefficient in cylindrical pores is defined as $\phi_{i,\mathrm{S}} \triangleq (1-\lambda_i)^2$ for solute i. The dielectric exclusion coefficient is decomposed into a product of $\phi_{i,\mathrm{B}}$ and $\phi_{i,\mathrm{im}}$, which account for the Born dielectric effect and the contribution of the fictitious image forces that arise at the membrane interface, respectively. The Born contribution is calculated as follows:

$$\phi_{i,\mathrm{B}} = \exp\left[-\frac{1}{k_B T}\frac{z_i^2 q^2}{8\pi\varepsilon_0 r_i}\left(\frac{1}{\zeta_p}-\frac{1}{\zeta_b}\right)\right] \tag{4}$$

where q, ε_0, k, and r_i are the fundamental electronic charge, permittivity of free space, Boltzmann constant, and Stokes radius of species i, respectively. In addition, ζ_p and ζ_b correspond to the dielectric constant in the membrane pores and the fluid bulk, respectively. A value of $\zeta_b = 78.54$ is used for all conducted studies.

$\phi_{i,\mathrm{im}}$ is quantified using analytical solutions to the cylindrical Poisson equation inside charged membrane pores, as derived by Yaroshchuk (Yaroshchuk, 2001):

$$\phi_{i,\mathrm{im}} = \exp\left[-\frac{2\alpha_i}{\pi k_B T}\int_0^\infty \frac{K_0(\kappa)K_1(\eta)-\tilde{\beta}(\kappa)K_0(\eta)K_1(\kappa)}{I_1(\eta)K_0(\kappa)+\tilde{\beta}(\kappa)I_0(\eta)K_1(\kappa)}d\kappa\right] \tag{5}$$

Here, I_0 and I_1 are zeroth and first order modified Bessel functions of the first kind. Similarly, K_0 and K_1 are zeroth order and first order Bessel functions of the second kind. These arise from the Fourier transform used to solve the Poisson equation in the cylindrical coordinate frame. In addition, k is the one-dimensional wave number and:

$$\alpha_i \triangleq \frac{1}{RT}\frac{z_i^2\mathfrak{F}^2}{8\pi\varepsilon_0\zeta_p N_A r_p} \tag{6}$$

$$\tilde{\beta} \triangleq \frac{k}{\sqrt{k^2+\mu^2}}\left(\frac{\zeta_p-\zeta_m}{\zeta_p+\zeta_m}\right) \tag{7}$$

Here, N_A is Avogadro's constant and ζ_m is the dielectric constant of the membrane matrix. Polyamide membranes tend to have dielectric constants in the range of 3-6 (Szymczyk and Fievet, 2005; Zhu et al., 2019a). A value of $\zeta_m = 4.5$ was used for all performed tests. Lastly, $\eta \triangleq \sqrt{k^2+\mu^2}$, where μ is expressed as:

$$\mu = r_p\left(\frac{\mathfrak{F}^2}{\varepsilon_0\zeta_b RT}\frac{I_b}{I}\sum_{i=1}^{N_s}\left[\frac{\gamma_i(0^-)}{\gamma_i(0^+)}z_i^2 C_{i,f,m}(0^-)\phi_{i,\mathrm{S}}\phi_{i,\mathrm{Di}}\phi_{i,\mathrm{Do}}\right]\right)^{1/2} \tag{8}$$

Here, I_b is the solution's ionic strength on the feed-side, while I is the ionic strength in the membrane. Additionally, N_s corresponds to the total number of ions in solution. Since $\phi_{i,\mathrm{im}}$ is an implicit function, these expressions must be solved iteratively to determine the image charge contribution.

The above equations are combined with the electroneutrality constraints in the membrane active layer as follows:

$$\sum_{i=1}^{N_s}\left[\frac{\gamma_i(0^-)}{\gamma_i(0^+)}z_i^2 C_{i,f,m}(0^-)\phi_{i,\mathrm{S}}\phi_{i,\mathrm{Di}}\phi_{i,\mathrm{Do}}\right] + \chi_d = 0 \tag{9}$$

where χ_d is the volumetric membrane charge density. If adsorption isotherms for the mixture are known, a composition-dependent charge density can be used in place of the above equation (Déon et al., 2011).

Lastly, the Donnan contribution to ion selectivity is given by:

$$\phi_{i,\mathrm{Do}} = \exp\left(-\frac{z_i\mathfrak{F}}{k_B T}\Delta\psi_{\mathrm{D},f}\right) \tag{10}$$

Here, $\Delta\psi_{\mathrm{D},f}$ corresponds to the Donnan potential on the feed-side. A mirrored expression is used in the permeate stream.

To close the system of equations, two additional electroneutrality constraints are needed (Rehman et al., 2021): one in the feed-side boundary layer and another in the permeate stream:

$$\sum_{i=1}^{N_s} z_i C_{i,f,m} = 0 \tag{11}$$

$$\sum_{i=1}^{N_s} z_i C_{i,p,b} = 0 \tag{12}$$

Here, we use the Pitzer-Kim multi-electrolyte model to evaluate activity coefficients, as it has shown far stronger agreement with experimental data than the often-used Davies model (Nagy et al., 2021; Pitzer, 1973). In the limit of dilute solutions, the Pitzer-Kim model converges to Davies model (Mistry et al., 2013). The details of the Pitzer-Kim model and its validation are provided in Appendix A.

Combining these equations, the model is solved iteratively, while minimizing three different electroneutrality residuals and an electric potential residual. To avoid numerical instabilities that introduce oscillations and/or divergence in simulation, we introduce under-relaxation to ensure numerical convergence across all analyses (Chapra and

Canale, 2001). Values of the under-relaxation factor varied between 0.01 to 0.95 across experiments, depending on the steepness of gradients present in the measured rejection.

2.4. Learning Pore Size through Expectation-Maximization

In prior work, we have applied maximum likelihood estimation (MLE) to formulate the objective function presented in Eq. (13) (Rehman and Lienhard, 2022). This formulation maximizes the likelihood of the observed data across a set of latent variables (governing yet hidden membrane parameters), $\mathcal{L} = \{r_p, \Delta x_e, \zeta_p, \chi_d\}$. The objective function, $f_{\text{obj}} : \mathbb{R}^{N_s \times N_w} \to \mathbb{R}$, where N_w is the total number of water flux measurements taken.

$$\mathcal{L}^* = \underset{\mathcal{L}}{\text{argmin}} \frac{1}{N_s N_w} \sum_{i=1}^{N_s} \sum_{j=1}^{N_w} \frac{(\mathfrak{R}_{i,j}^{\text{mod}} - \mathfrak{R}_{i,j}^{\text{exp}})^2}{\sigma_{i,j}^2} \tag{13}$$

Here, $\mathfrak{R}_{i,j}^{\text{mod}}$ and $\mathfrak{R}_{i,j}^{\text{exp}}$ are model and experimental rejections, respectively. $\sigma_{i,j}^2$ is the variance estimate of each experimental observation across multiple experimental trials. Iteration indices i and j cycle through all charged species experiments and flux measurements, respectively. $\mathcal{L}^*$ denotes the optimal set of latent parameters found.

Estimating the pore size distribution using Eq. (13) alone can become computationally intractable, as repetitive sampling is needed at each iteration of the optimization. The expectation-maximization (EM) algorithm is a probabilistic method well-suited to addressing this concern by iteratively maximizing the expectation of the marginal log likelihood conditioned on a given prior estimate (Dempster et al., 1977). To formulate this method, we define Q, the expected log likelihood function of $\hat{\theta}$: the parametrization of the pore size distribution, $\hat{\theta} = \{\hat{\mu}_r, \hat{\sigma}_r^2\}$:

$$Q \triangleq Q(\hat{\theta}|\hat{\theta}^{(t)}) = Q(\hat{\mu}_r, \hat{\sigma}_r^2 | \hat{\mu}_r^{(t)}, \hat{\sigma}_r^{2(t)}) \tag{14}$$

where $\hat{\mu}_r$ and $\hat{\sigma}_r^2$ are the mean and variance of the pore size distribution. Superscript (t) denotes the t^{th} iteration of the EM algorithm.

The first step of the EM algorithm is the expectation step, such that:

$$Q = \mathbb{E}_{r_p|\mathfrak{R}^{\text{exp}},\hat{\theta}^{(t)}} \left[\ln p(\mathfrak{R}^{\text{exp}}, r_p|\hat{\theta})\right] \tag{15}$$

Here, $p(\cdot)$ is the probability density function. Expanding the expectation yields:

$$Q = \int_0^\infty p(r_p|\mathfrak{R}^{\text{exp}}, \hat{\theta}^{(t)}) \ln p\left(\mathfrak{R}^{\text{exp}}, r_p|\hat{\theta}\right) dr_p \tag{16}$$

Since the pre-factor of the natural log is an unknown quantity, we can use the laws of conditional probability and Bayes rule to rearrange the relations:

$$p(r_p|\mathfrak{R}^{\text{exp}}, \hat{\theta}^{(t)}) = \frac{p(\mathfrak{R}^{\text{exp}}|r_p, \hat{\theta}^{(t)}) p(r_p|\hat{\theta}^{(t)})}{p(\mathfrak{R}^{\text{exp}}|\hat{\theta}^{(t)})} \tag{17}$$

The denominator of Eq. (17) is the marginal probability of the observed data (having integrated across all feasible values of pore size):

$$p(\mathfrak{R}^{\text{exp}}|\hat{\theta}^{(t)}) = \int_0^\infty p(\mathfrak{R}^{\text{exp}}|\tilde{r}_p, \hat{\theta}^{(t)}) p(\tilde{r}_p|\hat{\theta}^{(t)}) d\tilde{r}_p \tag{18}$$

Since the marginal probability is independent of r_p, it serves as a constant normalization factor for a given $\hat{\theta}^{(t)}$. Consequently, we refer to this factor as $\tau = \tau(\hat{\theta}^{(t)})$. For a given iteration of the EM algorithm, Gauss-Kronrod quadrature is used to compute τ. Combining the results, we obtain:

$$Q = \frac{1}{\tau} \int_0^\infty p(\mathfrak{R}^{\text{exp}}|r_p, \hat{\theta}^{(t)}) p(r_p|\hat{\theta}^{(t)}) \ln p(\mathfrak{R}^{\text{exp}}, r_p|\hat{\theta}) dr_p \tag{19}$$

Next, we can substitute the conditional probability relations from Eq. (17) back into the natural logarithm's argument to obtain the following:

$$\frac{1}{\tau} \int_0^\infty p(\mathfrak{R}^{\text{exp}}|r_p, \hat{\theta}^{(t)}) p(r_p|\hat{\theta}^{(t)}) \ln p(\mathfrak{R}^{\text{exp}}|r_p, \hat{\theta}) p(r_p|\hat{\theta}) dr_p \tag{20}$$

In this formulation, the arguments of the natural log are variable; however, the probabilities in the pre-factors are all computed using values from the previous iteration. The general form of Q resembles the negative of the Gibbs entropy commonly observed in statistical thermodynamics, in line with conventional MLE objective functions.

To compute $p\left(r_p|\hat{\theta}\right)$, we assert that the pore sizes in NF membranes conform to a log-normal distribution, as frequently observed in the literature (Bowen et al., 1997; Bowen and Welfoot, 2002b). This conformity is not a strict requirement for the model's applicability: as long as a distribution of pore sizes exists and can be sampled, this estimation technique applies. Since the log-normal probability density function is well-defined, we can evaluate this quantity as follows:

$$p(r_p|\hat{\theta}) = p(r_p|\hat{\mu}_r, \hat{\sigma}_r^2) \triangleq \frac{1}{r_p \hat{\sigma}_x \sqrt{2\pi}} \exp\left[-\frac{(\ln r_p - \hat{\mu}_x)^2}{2\hat{\sigma}_x^2}\right] \tag{21}$$

where $\hat{\mu}_x$ and $\hat{\sigma}_x^2$ (defined below) are the normalized values of $\hat{\mu}_r$ and $\hat{\sigma}_r^2$ in $p(\cdot)$. Note, other formulations of the log-normal distribution can be used in place of Eq. (21), as they are considered equivalent (Gaddum, 1945; Sutariya and Karan, 2022).

$$\hat{\mu}_x = \ln\left(\frac{\hat{\mu}_r^2}{\sqrt{\hat{\mu}_r^2 + \hat{\sigma}_r^2}}\right) \qquad \hat{\sigma}_x^2 = \ln\left(1 + \frac{\hat{\sigma}_r^2}{\hat{\mu}_r^2}\right) \tag{22}$$

To calculate $p\left(\mathfrak{R}^{\text{exp}}|r_p, \hat{\theta}\right)$, we use a slightly modified version of the MLE formulation reported in Eq. (13):

$$p\left(\mathfrak{R}^{\text{exp}}|r_p, \hat{\theta}\right) = \left(\frac{1}{\tau}\right) \exp\left[-\frac{1}{N_s N_w} \sum_{i=1}^{N_s} \sum_{j=1}^{N_w} \frac{(\mathfrak{R}_{i,j}^{\text{mod}} - \mathfrak{R}_{i,j}^{\text{exp}})^2}{\sigma_{i,j}^2}\right] \tag{23}$$

Here, the $1/\tau$ pre-factor arises from normalizing the probability across all feasible values of r_p. Formulating the approach in this way simplifies the mathematics for two reasons: (**1**) the product of the two functions in the natural log argument from Eq. (20) permits the exponents to be added; and (**2**) by taking the natural log of the resultant exponentials, we can optimize over a polynomial expression in the integral rather than a more complex logarithmic or exponential one.

These functions can be substituted back into Eq. (20). The second step of the EM algorithm is the maximization step. During the substitution, a negative sign appears in front of Q, which can be removed to convert the function to a minimization problem instead:

$$\hat{\theta}^{(t+1)} = \underset{\hat{\theta}}{\text{argmin}} \frac{1}{\tau^2} \int_0^\infty \tilde{\Xi}(\hat{\theta}^{(t)}) \exp\left(-\tilde{\Omega}_1(\hat{\theta}^{(t)}) - \tilde{\Omega}_2(\hat{\theta}^{(t)})\right) \left[\tilde{\Omega}_1(\hat{\theta}) + \tilde{\Omega}_2(\hat{\theta}) - \ln\left(\frac{\tilde{\Xi}(\hat{\theta})}{\tau}\right)\right] dr_p \tag{24}$$

Here, $\hat{\theta} = \hat{\theta}(r_p)$ and the values for $\tilde{\Xi}(\hat{\theta})$, $\tilde{\Omega}_1(\hat{\theta})$, and $\tilde{\Omega}_2(\hat{\theta})$ are:

$$\tilde{\Xi}(\hat{\theta}) \triangleq \frac{1}{r_p \hat{\sigma}_x \sqrt{2\pi}} \tag{25}$$

$$\tilde{\Omega}_1(\hat{\theta}) \triangleq \frac{1}{N_s N_w} \sum_{i=1}^{N_s} \sum_{j=1}^{N_w} \frac{(\mathfrak{R}_{i,j}^{\text{mod}} - \mathfrak{R}_{i,j}^{\text{exp}})^2}{\sigma_{i,j}^2} \tag{26}$$

$$\tilde{\Omega}_2(\hat{\theta}) \triangleq \frac{\left(\ln r_p - \hat{\mu}_x\right)^2}{2\hat{\sigma}_x^2} \tag{27}$$

This formulation also makes intuitive sense: (**1**) the terms in the exponentials are fixed at a given iteration, (t), and do not directly contribute to the complexity of the optimization; and (**2**) the trade-off between $\tilde{\Omega}_2(\hat{\theta})$ and $\ln(\tilde{\Xi}(\hat{\theta})/\tau)$ prevents the variance of the pore sizes from increasing boundlessly. These two terms arise from the log-normal distribution and serve as counterweights to one another: larger pore size variances decrease $\tilde{\Omega}_2(\hat{\theta})$, but conversely increase $\ln(\tilde{\Xi}(\hat{\theta})/\tau)$. The trade-off, in conjunction with $\tilde{\Omega}_1(\hat{\theta})$, which clearly resembles Eq. (13), is minimized as part of the EM algorithm. The optimization is performed recursively until $|(\hat{\theta}^{(t+1)} - \hat{\theta}^{(t)})/\hat{\theta}^{(t)}| < \varepsilon$, for $\varepsilon = 1 \times 10^{-4}$ across all conducted tests.

To evaluate $\hat{\theta}^{(t+1)}$, we use the downhill simplex optimizer as it was found to provide the fastest convergence properties for the proposed regression. In addition, in Appendix B, we prove that maximizing $Q(\hat{\theta}|\hat{\theta}^{(t)})$ leads to a direct improvement in the likelihood estimation for the pore size distribution.

2.5. Bilevel Optimization for Latent Parameter Estimation

For a given increase in $Q(\hat{\theta}|\hat{\theta}^{(t)})$ to yield a more likely pore size distribution, the remaining latent variables, $\{\Delta x_e, \zeta_p, \chi_d\}$, must remain constant across EM iterations. Since this assumption may not be justified, we propose a bilevel optimization problem that combines Eq. (13) with Eq. (24).

In the bilevel problem, the upper level optimization problem uses global optimization to attempt the MLE problem; however, at each iteration, the chosen set of latent variables serve as informed initial guesses to the EM procedure. Consequently, at each iteration of the upper level problem, the lower level optimization solves EM to determine the best pore size distribution for the current guess of latent variables. This process is repeated until convergence:

$$\begin{aligned} &\underset{\mathcal{L}}{\text{argmin}} \ \frac{1}{N_s N_w} \sum_{i=1}^{N_s} \sum_{j=1}^{N_w} \frac{(\mathfrak{R}_{i,j}^{\text{mod}} - \mathfrak{R}_{i,j}^{\text{exp}})^2}{\hat{\sigma}_{i,j}^2} \\ &\text{s.t.} \ \underset{\hat{\theta}}{\text{argmin}} \ \frac{1}{\tau^2} \int_0^{\infty} \tilde{\Xi}(\hat{\theta}^{(t)}) \exp\left(-\tilde{\Omega}_1(\hat{\theta}^{(t)}) - \tilde{\Omega}_2(\hat{\theta}^{(t)})\right) \\ &\qquad \left[\tilde{\Omega}_1(\hat{\theta}) + \tilde{\Omega}_2(\hat{\theta}) - \ln\left(\frac{\tilde{\Xi}(\hat{\theta})}{\tau}\right)\right] dr_p \end{aligned} \tag{28}$$

This approach allows us to efficiently determine the full set of latent variables, $\mathcal{L}^* = \{r_p, \Delta x_e, \zeta_p, \chi_d\}$, as well as the membranes pore size distribution, $\hat{\theta} = \{\hat{\mu}_r, \hat{\sigma}_r^2\}$, using only charged species data. In addition, this approach also eliminates the need for any explicit water flux relationships, such as the Hagen-Poiseuille equation to relate pore size and water flux (Rehman and Lienhard, 2022). Lastly, by learning the pore size distribution, we can apply quasi-Monte Carlo techniques to propagate the uncertainty into ion rejection, exclusion mechanisms, and ionic driving forces across our data.

3. Results and Discussion

3.1. Model Validation and Predictive Performance

To illustrate our framework's predictive performance, it is benchmarked against eight independent sets of experimental data spanning over 500 multicomponent measurements (Fig. 2A). The error bars in the modelled rejection stem from the propagation of the learned pore size distributions. The error bars in the experimental rejection arise through averaging rejection measurements across experimental trials. A $\pm 15\%$ error bound is indicated to signify the strong agreement between model and experiments across studied data. These findings assert the model's predictive capacity across datasets with diverse salinities, compositions, and membrane types[2].

A sample analysis is presented in Fig. 2B. The regressed values of the latent variables $\{\Delta x_e, \zeta_p, \chi_d\}$ are 1.16 µm, 43.86, and −63.0 mol/m^3, respectively. The values obtained by Micari et al. for the same set of parameters are 0.80 µm, 42.50, and −50.0 mol/m^3 (Micari et al., 2020). For NF270, the effective thickness typically ranges between 1–1.3 µm; measurements of 1.0 µm, 1.10 µm, and 1.21 µm, have all been previously reported by Bargeman et al., Kong et al., and Semião et al., respectively (Bargeman et al., 2014; Kong et al., 2016; Semião et al., 2013). This range aligns more closely with our set of parameters than those from the conventional regression methodology employed by Micari et al. For the pore dielectric constant, literature values typically range between 35–45 for NF270 (Oatley et al., 2012; Roy et al., 2015; Labban et al., 2018a). Our regressed values and Micari et al.'s studies are in close agreement and align well with the expected ranges from prior research. As the confined water molecules in the nanopores take on constrained orientations, the ability to respond to external electric fields is diminished, which leads to a reduction in the dielectric constant relative to the bulk (Oatley et al., 2012). Lastly, the membrane charge density is known to vary drastically as a function of solution chemistry and pH; charge densities for NF270 in the literature range between −150 mol/m^3 and −35 mol/m^3 at pH 7 for seawater salinities with solutions comprising of Na^+, Ca^{2+}, Mg^{2+}, Cl^-, and SO_4^{2-} (Hussain et al., 2008). In this work, our regressed parameters and those reported by Micari et al. fall into the expected range, further justifying the validity of our framework (Micari et al., 2020).

In addition to accurate parameter estimation, our approach also does not need access to uncharged solute data, pure water permeability measurements, or single salt studies at the membrane's isoelectric point (IEP), unlike conventional characterization procedures. We also achieve this result while attaining substantially lower optimization residuals than existing regression methods (Rehman and Lienhard, 2022)[3]. Previously, Micari et al. noted a 15% mean absolute deviation against their experimental data using classical DSPM-DE (Micari et al., 2020). We achieve a 6% mean absolute deviation. This improvement in error is consistently observed across all studied datasets with mean deviation improvements ranging between 5–15%.

Our approach also eliminates the assumption of independence between latent variables – conventional characterization procedures

[2] The model's key assumptions are summarized in Appendix C.

[3] In the worst case, our method will discover a set of membrane parameters that are equal to those obtained from the conventional characterization method (since these solutions still satisfy a local optimality condition). Note, in certain cases where classical DSPM-DE fails to identify sufficiently accurate results (i.e. solutions that don't regress well to data or those with unphysical latent parameters), our approach may succeed, but this is not strictly guaranteed.

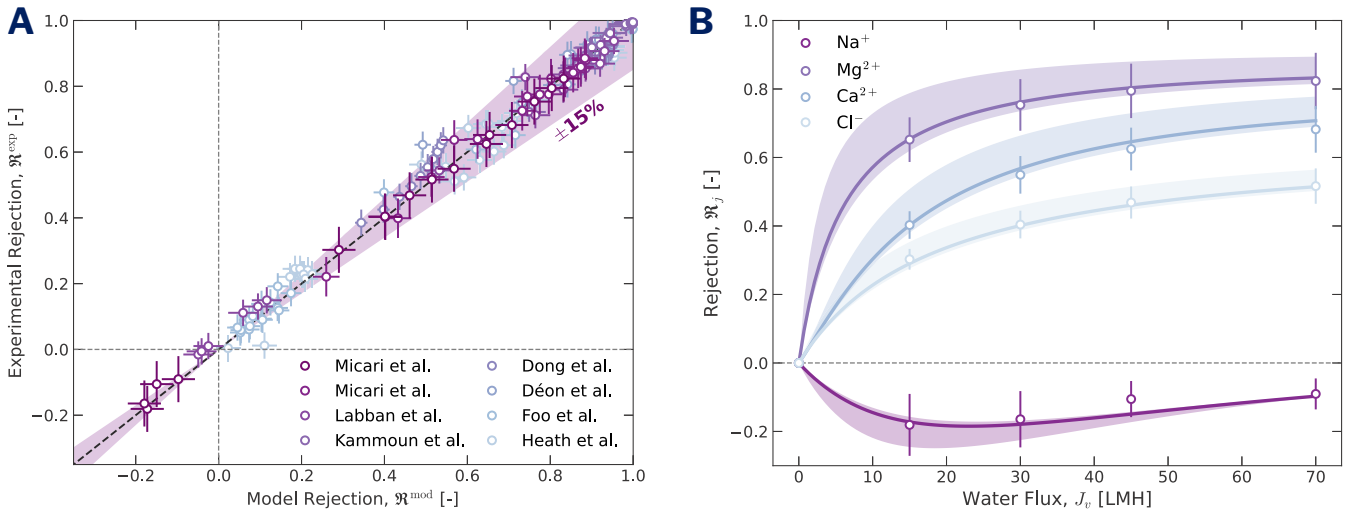

Figure 2: **(A)** A parity plot to illustrate the agreement between the model and experiments across all eight sets of experimental data. Values closer to the $y = x$ line indicate stronger alignment between the model and experiments; 95% of measured points fall within the ±15% error bounds. Ions present within the eight studied sourcewaters include: Na^+, K^+, Li^+, Ca^{2+}, Mg^{2+}, Cl^-, SO_4^{2-}, and NO_3^-. **(B)** Ion rejection as a function of water flux against data by Micari et al. (Micari et al., 2020). The pore size distributions obtained through the bilevel optimization and EM algorithm are passed into the computational model to characterize model uncertainty, which is represented by the shaded regions.

assume parameters remain unchanged after each set of characterization tests despite changes to solute choice, solution composition, and pH across experiments (we detail the conventional characterization procedure in Appendix D). This assumption is unlikely to generalize: for example, the swelling and de-swelling of polyamide membranes in the presence of alternate solutes or varying pH remains a subject of study (Cheng et al., 2018; Puhan et al., 2022). Consequently, propagating fixed values of Δx_e from pure water permeability tests to single salt studies at the IEP may be unphysical. Another example is that of pore constriction commonly observed at lower pH (Nghiem and Hawkes, 2007); this phenomena is also not accounted for by conventional methods. Previous studies conducted by Wang and Lin have reinforced these concerns: their findings suggest that a ±10% uncertainty in r_p can propagate to a ±20% uncertainty in Δx_e from experimental characterization alone (Wang and Lin, 2021). Similarly, a ±10% uncertainty in Δx_e can lead to ±10% uncertainty in χ_d from uncertainty propagation through experimental characterization (Wang and Lin, 2021). In the worst case, a ±10% uncertainty in ζ_p can lead to a ±100% uncertainty in χ_d. By employing the new regression framework, we relax the independence constraint and allow all latent variables to vary with composition and pH, resolving these concerns.

3.2. *Distribution Learning and Quasi-Monte Carlo Sampling*

By combining our global optimization method with EM, we are able to infer the membranes' pore size distributions. In Fig. 3A, the lower level EM procedure for different initial estimates of the pore size mean and standard deviation is demonstrated for NF270. The values on the x- and y-axis represent initial guesses for the mean and standard deviation, respectively. The joint probability distribution functions are characterized using Gaussian smoothing functions and signify the most frequently converged to Gaussian statistics. For a given initial guess, (μ_0, σ_0), a sample trajectory is provided, where the most likely pore size mean and standard deviation are 0.50 nm and 0.13 nm, respectively, for NF270, as denoted by the '$*$'.

Our determined pore size of 0.50 nm is very close to the computationally-derived 0.51 nm value reported by Micari et al. (Micari et al., 2020). Both these values also agree closely with experiments for NF270 that indicate a mean pore size range of 0.43–0.54 nm (Oatley et al., 2012; Dalwani et al., 2011). Hilal et al. previously attempted to ascertain the pore size distribution of NF270 membranes using atomic force microscopy (AFM); however, since the inherent uncertainty of determining pore size through AFM measurements can become substantial, they obtained relatively large means and standard deviations (Hilal et al., 2005)[4]. For NF270, a mean and standard deviation of 0.68 nm and 0.23 nm were measured, respectively (Hilal et al., 2005). Since AFM only interacts with the surface of the polyamide membrane, it can be challenging to discern whether depressions in the membrane morphology are due to pores or dimples in the polymer matrix. Wang et al., Li et al., and He et al., have all tried to combine cascades of neutral solute experiments to regress the pore size distribution of NF270 using molecular weight cutoff (MWCO) measurements. Applying this approach, they have obtained standard deviation ranges between 0.08–0.18 nm, which are in close agreement with the 0.13 nm value derived from our approach (Wang et al., 2014; Li et al., 2019; He et al., 2022). In addition, the mean pore radii obtained through their studies were in the range of 0.42–0.57 nm, which agree well with our value of 0.50 nm. Košutić et al. used an alternate approach to characterize the pore size distributions of NF membranes using the surface-force pore flow model (Košutić et al., 2005). This method yielded a standard deviation of 0.12 nm for NF270, which also agrees very well with the values quantified in our work. These findings support the use of our method in inferring pore size distributions from charged solute data alone.

In Fig. 3B, for two sets of data, ion rejection distributions are demonstrated at a fixed flux of $J_v = 15$ LMH. Here, quasi-Monte Carlo sampling using non-discepancy Sobol sequences is used to propagate the derived pore size distributions through the model and

[4]For more details, Sutariya et al. provide an extensive study contrasting different approaches for quantifying pore size distributions in NF membranes (Sutariya and Karan, 2022).

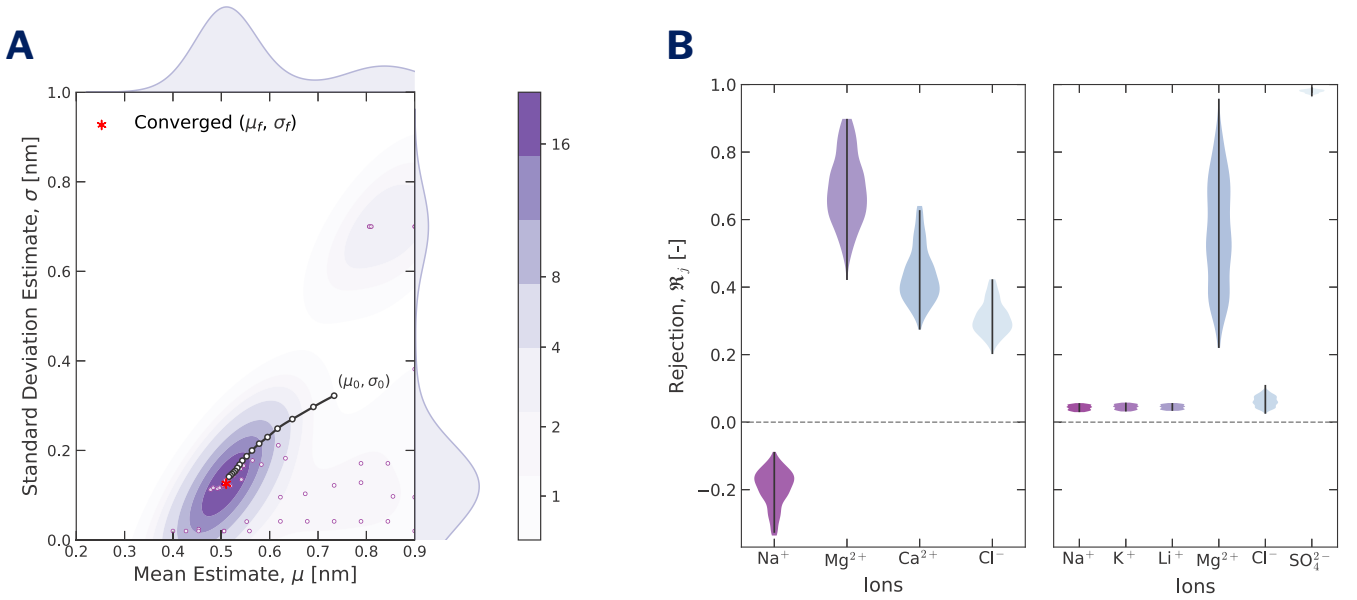

Figure 3: **(A)** For different initial estimates of the mean and standard deviation informed from the upper level global optimization problem, the EM algorithm searches for the most likely pore size distribution using the Micari et al. dataset. Converged values, marked by the red asterisks, correspond to $\hat{\mu}_r$ and $\hat{\sigma}_r$ of 0.50 nm and 0.13 nm, respectively. **(B)** For two different sets of experimental data (left-hand-side uses Micari et al.'s compositions and right-hand-side uses Foo et al.'s compositions), the pore size distributions are propagated through the computational architecture using a quasi-Monte Carlo approach (Micari et al., 2020; Foo et al., 2023). These results elucidate the sensitivity of ionic rejection and selectivity at a fixed flux $J_v = 15$ LMH to a distribution of membrane pore sizes.

quantify the uncertainty in ion rejection. The datasets regressed correspond to those obtained by Micari et al. and Foo et al. in the left and right sub-panels, respectively (Micari et al., 2020; Foo et al., 2023). In both cases, the ion rejection is asymmetric about the expected value, in alignment with the log-normal probability density function[5]. Here, we note the large range in ion rejection values observed for different values of pore size. Using Micari et al.'s composition, the Mg^{2+} rejection can be as low as 0.42 and as high as 0.90. Similarly, the Ca^{2+} and Na^{+} rejections range between 0.27 to 0.62 and -0.35 to -0.10, respectively. Although the expected selectivity of Ca^{2+}/Na^{+} is around 1.98, it can be as low as 1.51 and as high as 3.46 from pore size distribution contributions alone. For Mg^{2+}/Na^{+}, the expected selectivity is 3.39; however, it can take values from 1.89 all the way up to 13.5. These wide ranges underscore the importance of integrating pore size distributions into NF transport models to better quantify the expected range of measured selectivities.

Furthermore, the relatively similar areas of the violin plots for Micari et al.'s data suggest that differences in pore size impact all ions in solution similarly. This does not have to be the case, as observed in the right sub-panel. In the case of Micari et al.'s data, the driving factor is the similar relative initial concentrations of all cations. Since Na^{+} has the least sensitivity to pore size compared to other cations (it has the smallest Stokes radius relative to the other cations and a lower effective charge), decreases in pore size first elevate the rejection of the divalent species, which in turn, induces a pronounced passage of Na^{+} to enforce electroneutrality. This explains Na^{+}'s negative rejection at lower pore sizes and the mirrored distribution Na^{+} exhibits relative to the other ions (a reflection in the x-axis) (Labban et al., 2017; Yaroshchuk, 2008).

[5]There is some additional warping of the distribution because of the highly non-linear mapping that the framework encodes to satisfy boundary conditions and enforce electroneutrality.

In the case of Foo et al.'s data, variation over the distribution of pore sizes impacts all ions, but primarily Mg^{2+}. In this case, the relative concentrations of all the cations are quite dissimilar. Furthermore, since Mg^{2+} is the largest cation and the only divalent one in solution, it is the most sensitive solute to all three selectivity mechanisms: steric, dielectric, and Donnan exclusion. Consequently, when pore size decreases, the rejection values of the monovalent metal ions are not significantly impacted, whereas Mg^{2+} rejection varies to a large extent. Note that the relative concentration of Mg^{2+} in solution is small compared to the other ions, and consequently, large changes in Mg^{2+} rejection do not necessitate large changes in anion rejection to maintain electroneutrality (Yaroshchuk, 2008).

We also observe that Cl^{-} appears to be more sensitive to changes in cation rejection than SO_4^{2-}. This aligns with expectation for two reasons: (**1**) SO_4^{2-} has a larger Stokes radius than Cl^{-}, leading to higher steric rejection rates relative to Cl^{-}; and (**2**) since SO_4^{2-} is a divalent anion, the negatively-charged NF270 membrane (at pH 7) screens SO_4^{2-} more effectively than Cl^{-}. This difference in membrane charge is also consistent with Mg^{2+} being more impacted than SO_4^{2-} at lower pore radii, given that they are both large hydrated ions with divalent yet opposing charge.

For lithium recovery, the large uncertainty noted for Mg^{2+} can have significant implications. One of the main metrics used to ascertain NF performance is Li^{+}/Mg^{2+} selectivity. If the uncertainty in magnesium rejection is substantial, large uncertainties propagate into ion selectivity. The resulting estimates of selective performance can be highly conservative, or worse, large overestimates of ion separation. In this case, the expected Li^{+}/Mg^{2+} selectivity is 2.23; however, the lower bound and upper bound are 1.15 and 46.4, respectively. To better predict selectivity and its sensitivity for selective separations, the importance of uncertainty quantification in transport models is clear, as shown here.

3.3. Ablation Studies for Enhancing Selectivity

Ablation studies on ion rejection can elucidate the relative sensitivity of selective performance to the governing membrane parameters. These studies can also highlight the uncertainty that arises from pore size distribution effects on ion rejection across the expected ranges of the membrane parameters.

In Fig. 4A and 4B, we show the variation in ion selectivity and rejection as a function of independently-varied membrane charge density, while holding the dielectric constant and membrane thickness fixed for two sample datasets (Micari et al., 2020; Foo et al., 2023). The membrane charge density is the easiest membrane parameter to operationally control, as it can be modified post membrane fabrication (Labban et al., 2017). Polyelectrolyte deposition, grafting, and pH control, can all be used to tune the selectivity of polyamide membranes for various separations (Epsztein et al., 2015). In Fig. 4A, the vertical black dotted line represents the membrane charge density regressed from experimental studies at pH 7. Under these conditions, the NF270 membrane is hydrophilic and negatively-charged, which is consistent with zeta potential measurements at pH 7 (Ortiz-Albo et al., 2019; Pino-Soto et al., 2021). Consequently, based on charge effects alone, cations are drawn towards the membrane, while anions are repelled. Mg^{2+} and Ca^{2+} experience larger body forces than Na^+ due to their higher effective charge; however, their substantially larger Stokes radii relative to Na^+ ($r_{Mg^{2+}} = 0.347$ nm $> r_{Ca^{2+}} = 0.309$ nm $> r_{Na^+} = 0.184$ nm) means they are also more sensitive to steric effects (Hussain et al., 2007). Here, the steric effects appear to play a more dominant role in transport relative to Donnan exclusion: Mg^{2+} and Ca^{2+} exhibit high rejection rates despite the membrane's negative charge. Similarly, although Cl^- experiences electrostatic repulsion by the membrane, its relatively large hindered diffusion coefficient leads to substantial diffusive transport through the polyamide membrane. This process subsequently entrains Na^+ (the least sensitive cation) ions to meet the electroneutrality conditions, leading to the negative rejection of Na^+; a phenomenon that has been previously observed in the literature (Labban et al., 2017; Roy et al., 2015; Yaroshchuk, 2008). These results agree well with experimental observations illustrating the model's ability to capture ionic coupling for metal recovery applications (Micari et al., 2020; Roy et al., 2017; Roy and Lienhard, 2019).

As the membrane becomes more positively-charged (increasing values of χ_d), these effects become pronounced. Now, in addition to the substantial steric hindrance experienced by the divalent cations, the positively-charged membrane acts to repel them, further elevating their rejections, as suggested by Fig. 4A. The Donnan repulsion effects also become more notable for Na^+, leading to an inflection point in its rejection behaviour as membrane charge increases. The results noted for Cl^- are interesting, however, since they suggest that despite the membrane charge providing a lower resistance electrostatic pathway for Cl^-, the rejection still increases as the membrane tries to satisfy electroneutrality. This behaviour is a by-product of Cl^- being the only anion in the solution. In cases where other anions are present, competing effects between these anions can be observed that depend on initial concentration, hydrated ion size, and effective charge. These findings are consistent with experimental observations across the literature (Labban et al., 2017; Micari et al., 2020).

Lastly, in the Ca^{2+} and Mg^{2+} recovery case, with increasing membrane charge density, the rejection of the divalent cations increases, while the rejection of Na^+ decreases. Mathematically, $\frac{\partial \mathfrak{R}_{Mg^{2+}}}{\partial \chi_d} > 0$, $\frac{\partial \mathfrak{R}_{Ca^{2+}}}{\partial \chi_d} > 0$, while $\frac{\partial \mathfrak{R}_{Na^+}}{\partial \chi_d} < 0$. This suggests that the Mg^{2+}/Na^+ and Ca^{2+}/Na^+ selectivity can be enhanced by operating NF at reduced pH. In Fig. 4A, the optimal Mg^{2+} and Ca^{2+} selectivities are denoted by $\tilde{S}^{Mg^{2+}}_{Na^+}$ and $\tilde{S}^{Ca^{2+}}_{Na^+}$, respectively, where the trade-off between Donnan and steric effects is at an optimal value. For metal recovery applications, these findings suggest that Mg^{2+} and Ca^{2+} selectivities can potentially be increased by a factor of ~5.52x and ~3.04x, respectively. These studies agree well with literature findings, which have noted a 3–7x improvement in $\tilde{S}^{Ca^{2+}}_{Na^+}$ and $\tilde{S}^{Mg^{2+}}_{Na^+}$ selectivity at pH 2–4 for water softening applications (Epsztein et al., 2015; Nativ et al., 2021).

In the Li^+ recovery case, at pH 7, the monovalent cations are rejected in the order of their Stokes radii[6]. This aligns with expectation since all the monovalent cations experience the same magnitude Donnan effect, with nearly indistinguishable dielectric exclusion terms (taking the exponential of the Stokes radii leads to similarly consistent dielectric effects across monovalent cations). Consequently, the steric effects play a majority role in governing their rejection order, as noted with the Micari et al. data. The only divalent cation, Mg^{2+}, experiences substantially higher rejection than the monovalent cations, which can be attributed to its larger Stokes radius ($r_{Mg^{2+}}$ = 0.347 nm) and higher effective charge. For SO_4^{2-}, the rejection rates are higher than all the other cations at pH 7; in addition to its relatively large Stokes radius ($r_{SO_4^{2-}}$ = 0.231 nm), its large negative effective charge further repels it from the negatively-charged NF270 membrane. Consequently, Cl^-, albeit electrostatically repelled by the membrane, serves as the anion that maintains electroneutrality in the permeate stream. This can be attributed to three factors: (**1**) its high relative concentration in the incoming sourcewater relative to SO_4^{2-}; (**2**) its lower effective charge than SO_4^{2-}; and (**3**) its smaller Stokes radius relative to SO_4^{2-}. These learnings are consistent with those observed in the previous set of data and with findings across the literature for multicomponent solutions containing Cl^- and SO_4^{2-} (Micari et al., 2020; Foo et al., 2023; Labban et al., 2018b).

Furthermore, as seen with Ca^{2+} and Mg^{2+} recovery, Li^+/Mg^{2+} selectivity can be enhanced by operating the NF system at a reduced pH. Decreasing the pH increases the membrane charge density, making the membrane more positively-charged and increasing the Donnan screening of the cations. Cations with a higher effective charge are more impacted. In Fig. 4B, it can be noted that with increasing charge density, the rejection of Mg^{2+} increases far more significantly than that of Li^+ i.e. $\frac{\partial \mathfrak{R}_{Mg^{2+}}}{\partial \chi_d} > \frac{\partial \mathfrak{R}_{Li^+}}{\partial \chi_d}$. In this case, Li^+/Mg^{2+} selectivity can be increased by over an order of magnitude from 2.23 up to 34.1 ± 5.7. Our studies agree well with results obtained by Foo et al., where the experimental separation efficiency at pH 7 and pH 2 was 2.15 and 39.1, respectively (Foo et al., 2023). These values agree closely with our simulations. Our results demonstrate two learnings: (**1**) the model has the predictive ability to identify when pH control may or may not provide selectivity benefits for diverse mixtures; and (**2**) the model can accurately quantify the selectivity gains from pH optimization (Cheng et al., 2018; Puhan et al., 2022).

Next, in Fig. 4C and 4D, we provide a quantitative description of the impacts of independently-varying membrane thickness and pore radius on ion rejection, respectively, while holding the remaining latent parameters constant. Reductions in Δx_e correspond to membranes

[6] In order of decreasing rejection, $\mathfrak{R}_{Li^+} > \mathfrak{R}_{Na^+} > \mathfrak{R}_{K^+}$. This aligns with the Stokes radii order: $r_{Li^+} = 0.238$ nm $> r_{Na^+} = 0.184$ nm $> r_{K^+} = 0.125$ nm.

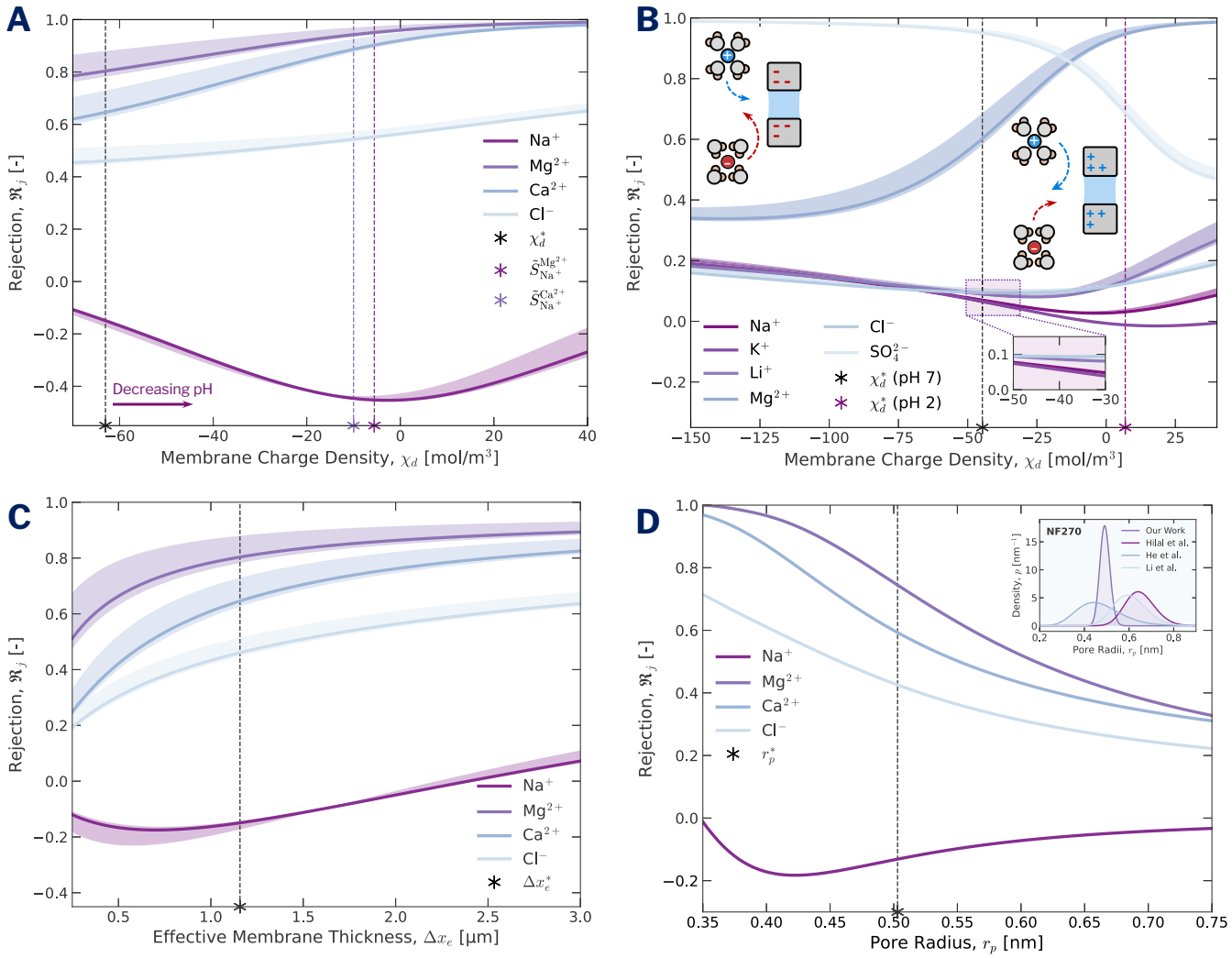

Figure 4: **(A)** The impact of modifying the membrane charge density on ion rejection. The value regressed to Micari et al.'s data is denoted by the dotted black line, while optimal values for maximum selectivity of Mg^{2+} and Ca^{2+} are denoted by the lilac and purples lines, respectively. **(B)** Ion rejection as a function of membrane charge density for the Li^+ recovery data. The dotted black line corresponds to the regressed value at pH 7, while the purple line is the regressed value at pH 2. Nearly an order of magnitude improvement in ion selectivity results from operating at a reduced pH. **(C)** Ion rejection as a function of effective membrane thickness. **(D)** The impact of tuning membrane pore radius on ion selectivity and rejection. The inset corresponds to the learned pore size distribution from our bilevel optimization framework and other experimental characterizations conducted on NF270 from the literature (Hilal et al., 2005; Wang et al., 2014; Li et al., 2019; He et al., 2022).

that are thinner, have a decreased tortuosity, and/or increased porosity. In Fig. 4C, the benefits of decreasing Δx_e are observed; however, the improvements do not appear to be as attractive as pH control for selectivity enhancement. Even accounting for the uncertainties from the quasi-Monte Carlo sampling, the Mg^{2+} and Ca^{2+} selectivity is only improved from 3.39 and 1.98 to 4.72 ± 0.45 and 2.36 ± 0.38, respectively. These incremental benefits suggest that designing thinner membranes with decreased tortuosity or heightened porosity might not be the optimal path forward for achieving high ion selectivity for metals recovery applications. These findings agree well with those noted by Labban et al., who also observed 15–20% improvements in hardness removal through membranes with reduced/optimized Δx_e values (Labban et al., 2017, 2018b).

During fabrication, membrane pores can be modified through processes like chemical cross-linking (Stair et al., 2001). Although chaotic processes like interfacial polymerization make it nearly impossible to obtain fixed pore sizes, by tuning the pore radius of the membranes, heightened metal ion selectivities can be achieved (Hao et al., 2023). This is also clearly observed in Fig. 4D. Although substantially more effective than modifying Δx_e, the improvements are still not as notable as those from tuning χ_d. At a reduced pore size of $r_p \approx 0.42$ nm, the values of $S_{Na^+}^{Mg^{2+}}$ and $S_{Na^+}^{Ca^{2+}}$ are 23.6 and 6.56, which are improvements of $7.0\times$ and $3.3\times$ for Mg^{2+} and Ca^{2+}, respectively, compared to $r_p = 0.50$ nm. The reduced pore size primarily impacts the divalent cations since they have substantially larger Stokes radii, while Na^+ is not as impacted. Bringing the divalent rejections closer to 1 leads to improved selectivities since Na^+ is already rapidly moving across the membranes. In addition, since the Stokes radius of Cl^- is smaller than that of Na^+ it is not be the first ion to be affected.

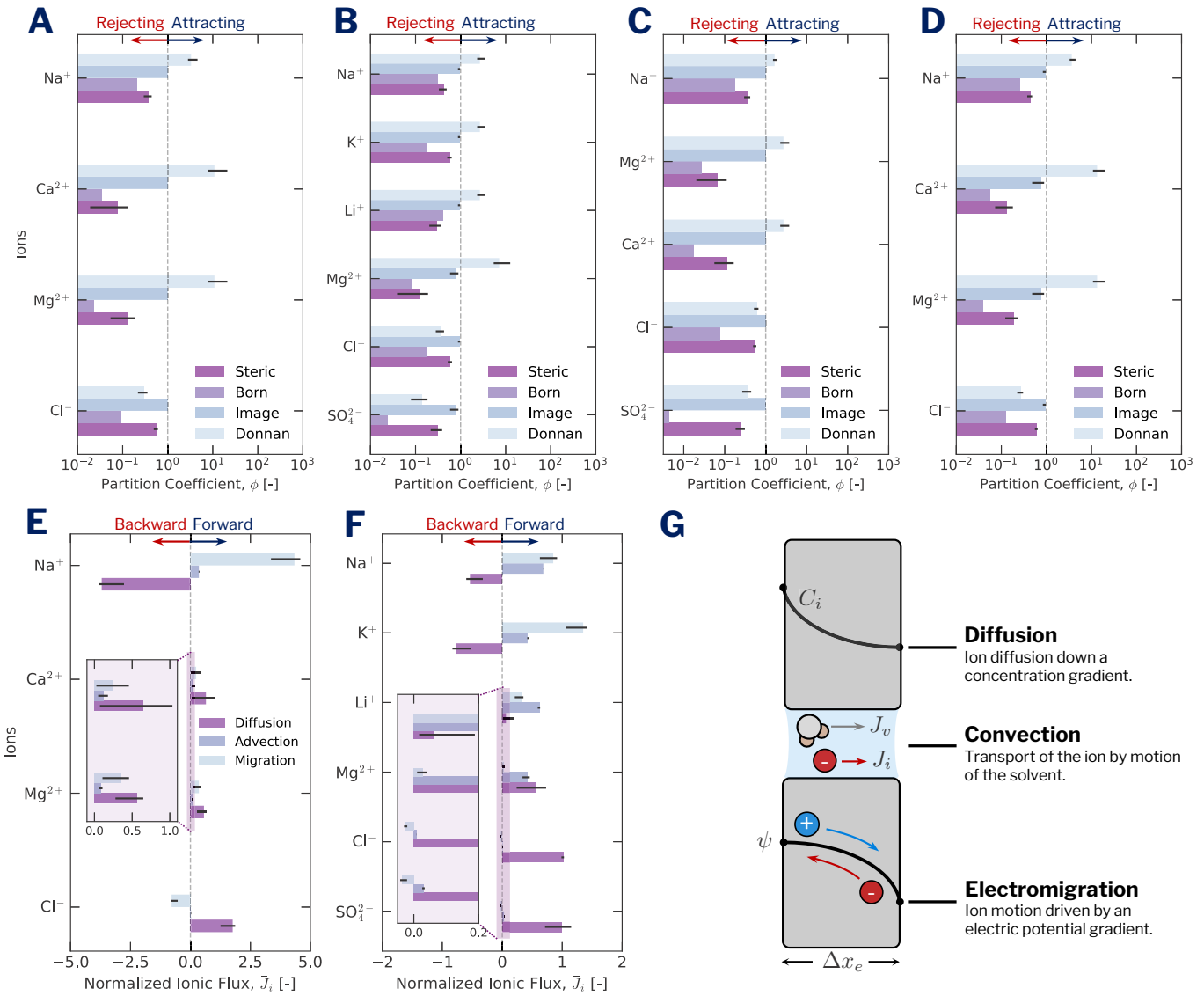

Figure 5: **(A)-(D)** Steric, Born, image, and Donnan partition coefficients for all ions in solution across four sample datasets (A: Micari et al. [NF270]; B: Foo et al. [NF270]; C: Labban et al. [LbL-1.5C]; D: Micari et al. [TS80]) (Labban et al., 2017; Micari et al., 2020; Foo et al., 2023). **(E)-(F)** The normalized flux with individual contributions for diffusion, convection, and electromigration, using two sample datasets (E: Micari et al. [NF270]; F: Foo et al. [NF270]) (Micari et al., 2020; Foo et al., 2023). **(G)** Diffusion, convection, and electromigration driving forces for multicomponent ion transport through the NF membrane.

3.4. Uncertainty in Partition Coefficients and Transport

Partition coefficients and ionic fluxes are often used to study selectivity mechanisms and driving forces for transport (Wang et al., 2021a; Ahmad and Ooi, 2010). Partition coefficients quantify the magnitude of a selectivity mechanism: values below 1 indicate a tendency to be repelled by the membrane, while values above 1 signify an attractive force. In Fig. 5, predicted partition coefficients and ionic fluxes, as well as their uncertainties are shown.

In Fig. 5A-D, four sample analyses are presented. In all cases, the Donnan partition coefficient, $\phi_{i,\mathrm{Do}}$, is larger than 1 for cations and below 1 for anions, in agreement with expectation for hydrophilic negatively-charged membranes[7]. In addition, ions with a larger effective charge exhibit more substantial screening/attractive effects. For example, in Fig. 5A, Ca^{2+} and Mg^{2+} experience larger attractive forces than Na^{+}, as suggested by $\phi_{Ca^{2+},\mathrm{Do}} > \phi_{Na^{+},\mathrm{Do}}$ and $\phi_{Mg^{2+},\mathrm{Do}} > \phi_{Na^{+},\mathrm{Do}}$. These findings are consistent across all datasets. The uncertainties noted in the Donnan partition coefficients are also provided, where multivalent ions exhibit larger sensitivities to pore size. Since different values of the pore radius lead to modified resultant electric potentials, ions with a higher effective charge are more readily impacted than those with a lower charge. Consequently, multivalent ions exhibit larger uncertainties in their Donnan partitioning coefficients compared to their monovalent counterparts; these findings are consistent with experimental observations from the

[7] In our study, we also noted that forcing the membrane charge density to be positive (i.e. signifying a positively-charged membrane) did lead to a reversal in the Donnan partition coefficients between cations and anions. This finding agrees with expectation given that at lower pHs the membrane is more effective at screening cations and drawing in anions.

literature (Ritt et al., 2020, 2022). Similar to the violin plots presented in Fig. 3B, the asymmetric uncertainties can also be attributed to the asymmetric log-normal pore size distribution used.

Another insight from the model is the non-overlapping error bars noted in the partition coefficients. Although it can be challenging to discern individual ion selectivity mechanisms, the uncertainties appear distinct enough to suggest dielectric exclusion (specifically the Born contribution) to be the predominant partitioning mechanism. Although the dielectric term in the model is typically seen as an over-simplification of the governing dynamics, experimental studies in the literature have consistently concluded that partial dehydration is likely the governing exclusion mechanism for ion selectivity in polyamide membranes (Pavluchkov et al., 2022; Zhai et al., 2022; Epsztein et al., 2018). Consequently, the model's prediction that dielectric exclusion is the most significant contributor to ion selectivity can be seen as representative of experimental observations. Note that these findings are only suggestive, and not prescriptive, given the complex nature of ion selectivity, and should be taken solely as the model's ability to provide insight consistent with experimental learnings rather than conclusive evidence of partitioning relationships.

Fig. 5A-D shows partition coefficients from the image force contributions. Molecular dynamics (MD) simulations have previously revealed that the role of image forces in ion selectivity may not be very significant, especially at the lower concentrations considered in this work (Wang and Ma, 2012; Zhu et al., 2019b; Fadaei et al., 2012). Our findings support these claims, where the image force partition coefficients quantified across all studied ions are consistently between 0.9–1, even with uncertainties propagated. Although the difference in dielectric constant between the membranes and the solvent is relatively large ($\zeta_m = 4.5 \ll \zeta_b = 78.54$), at low concentrations the repulsion from the polarized layer is small, as evidenced by the near unity partition coefficients. These findings are also consistent with Yaroshchuk's studies on dielectric exclusion in charged nanofiltration membrane pores, providing additional credibility to the model's predictive capabilities (Yaroshchuk, 2000, 2001; Yaroshchuk et al., 2019).

The uncertainty in ion fluxes, in Fig. 5E and 5F, show that there is substantial overlap between the diffusive, convective, and electro-migration terms across certain ionic species. In Fig. 5E, for Ca^{2+} and Mg^{2+}, overlap between all three driving forces is observed, and in Fig. 5F, overlap between the convective and diffusive contributions is noted for Mg^{2+}. These observations suggest that it may be misleading to conclude that one driving force is dominant over the other from the modelling framework alone. For the investigated situations, it is difficult to claim that Ca^{2+} and Mg^{2+} transport is primarily diffusive or that Li^{+} transport is governed by convective transport. What is clear is that changing pore radius has a direct impact on the flux contributions through the change in hindrance factors, as well as an indirect impact from the resultant electric potential fields needed to satisfy electroneutrality (Ahmad and Ooi, 2010; Fadaei et al., 2012). Consequently, a high degree of sensitivity of the ionic flux to pore size is observed. Lastly, these findings support the use of the presented computational framework to model transport and study partitioning trends to motivate studies ion selectivity; however, the findings also suggest that making claims around ion driving forces may lead to misleading conclusions.

4. Summary and Conclusions

In this work, we develop an ion transport model combined with probabilistic estimation techniques to quantify latent membrane parameters and their governing distributions. In addition, we combine the modelling framework with quasi-Monte Carlo sampling methods to quantify uncertainty in NF systems for metal recovery applications. Our main findings are:

1. Our developed approach can quantify the latent membrane parameters and pore size distributions using charged species data alone to within $\pm 15\%$ of multicomponent data from over 500 experimental measurements.
2. The proposed regression methodology relaxes the independence assumption made by conventional characterization methods, eliminating uncertainty propagation from the parameter estimation process; in contrast, errors in conventional efforts introduce $\pm 100\%$ uncertainties in latent membrane parameters.
3. Beyond parameter estimation, we have performed ablation studies to explore avenues for selectivity enhancement. Our studies show that pH optimization can provide selectivity improvements of 3–10$\times$, depending on the metals of interest. Here, we focused on Mg^{2+}, Ca^{2+}, and Li^{+} recovery from diverse sourcewaters. Our findings agree well with experiments from the literature.
4. Using our parametric analyses, our studies suggest that tuning pore size distributions and membrane thicknesses (either through decreases in tortuosity or increases in porosity) offer fewer benefits in selectivity enhancement than pH optimization.
5. Using quasi-Monte Carlo sampling with Sobol sequences, we propagated the learned pore size distributions through the model to study the sensitivity of partition coefficients and ion driving forces to pore size. With partition coefficients, our results suggest dielectric exclusion to be the predominant selectivity mechanism, in line with experimental observations.
6. The image force contributions appear to be small compared to the other partitioning mechanisms, in agreement with MD simulations (image force partition coefficients are consistently between 0.9–1 across salinities).
7. Finally, the regressed partition coefficients agree well with experimentally-determined values. In addition, the uncertainties in the magnitude of the ion driving forces are highly sensitive to the estimated pore radius making it challenging to draw conclusions about the dominant ion driving force.

5. Acknowledgements

The authors thank the Centers for Mechanical Engineering Research and Education at MIT and SUSTech (MechERE Centers at MIT and SUSTech) for partially funding the research reported here. Danyal Rehman acknowledges financial support provided by a fellowship from the Abdul Latif Jameel World Water and Food Systems (J-WAFS) Lab and fellowship support from the Martin Family Society of Fellows.

Nomenclature

Greek Symbols

α_i	Image Force Contribution Parameter for Solute i
$\tilde{\beta}$	Image Force Contribution Parameter
χ_d	Volumetric Membrane Charge Density
$\Delta\psi_{\mathrm{D}}$	Donnan Potential
Δx	Spacing on Chebyshev Collocation Grid
Δx_e	Effective Membrane Thickness
δ	Estimated Thickness of Layer of Water in Nanopores
ε	Convergence Tolerance for EM Algorithm
ε_0	Permittivity of Free Space
γ_i	Activity Coefficient of Solute i
λ	Order of Spectral Differentiation Operator
$\mathcal{L}$	Latent (Hidden) Membrane Parameters
$\mathcal{L}^*$	Optimal Latent (Hidden) Membrane Parameters
$\hat{\mu}_r$	Estimate of Pore Radius Mean
$\hat{\mu}_x$	Estimate of Normalized Pore Radius Mean
μ_i	Chemical Potential of Solute i
μ_w	Dynamic Viscosity of Water
ϕ	Osmotic Coefficient of Water
$\phi_{i,\mathrm{B}}$	Born Contribution Partition Coefficient of Solute i
$\phi_{i,\mathrm{Di}}$	Dielectric Exclusion Partition Coefficient of Solute i
$\phi_{i,\mathrm{Do}}$	Donnan Exclusion Partition Coefficient of Solute i
$\phi_{i,\mathrm{im}}$	Image Forces Partition Coefficient of Solute i
$\phi_{i,\mathrm{S}}$	Steric Exclusion Partition Coefficient of Solute i
ψ	Electric Potential
σ	Polyamide Membrane Surface Charge
$\hat{\sigma}_r$	Estimate of Pore Radius Standard Deviation
$\hat{\sigma}_x$	Estimate of Normalized Pore Radius Standard Deviation
$\sigma^2_{i,j}$	Estimate of Experimental Measurements Variance
τ	Normalization Constant in EM Algorithm
$\hat{\theta}$	Parameterization of Membrane Pores
ξ	Linearized Electric Potential Gradient
ζ_b	Dielectric Constant of Water in the Bulk Solution
ζ_m	Dielectric Constant of the Polyamide Membrane
ζ_p	Dielectric Constant in the Membrane Pores

Roman Symbols

0^+	Membrane Side at Solution-Membrane Interface (Feed)
0^-	Solution Side at Solution-Membrane Interface (Feed)
a	Activity
A^ϕ	One-third of Debye Limiting Gradient
C_i	Molar Concentration of Solute i
$\mathcal{D}_\lambda$	λ^{th}-order Spectral Derivative Operator (Collocation)
$\tilde{\mathcal{D}}_\lambda$	λ^{th}-order Spectral Derivative Operator (Coefficient)
D_i	Diffusion Coefficient of Solute i
F	Debye-Hückel Contribution Term
f_{obj}	Objective Function for Maximum Likelihood Estimation
$H_{i,c}$	Integrated Convective Hindrance Coefficient of Solute i
$H_{i,d}$	Integrated Diffusive Hindrance Coefficient of Solute i
I	Ionic Strength
I_0, I_1	Zeroth and First Order Bessel Functions of First Kind
$\bar{J}_i$	Normalized Molar Flux of Solute i
J_i	Molar Flux of Solute i
J_v	Permeate Water Flux
$\bar{k}_{c,i}$	Modified Mass Transfer Coefficient of Solute i
K_0, K_1	Zeroth and First Order Bessel Functions of Second Kind
k_B	Boltzmann's Constant
$K_{i,c}$	Convective Hindrance Coefficient of Solute i
$K_{i,d}$	Diffusive Hindrance Coefficient of Solute i
m	Ion Molality
N	Number of Discretization Points in Collocation Grid
N_A	Avogadro's Constant
N_s	Number of Solutes in Mixture
N_w	Number of Water Flux Measurements Taken
p	Probability Density Function
Pe_i	Péclet Number of Solute i
Q	Expectation of Complete Data (Measured and Latent)
q	Fundamental Electronic Charge
R	Universal Gas Constant
r_i	Stokes Radius of Solute i
r_p	Pore Radius of Membrane
S_X^M	Selectivity between Ion M and Ion X
T	Absolute Temperature
x	Spatial Coordinate Orthogonal to Membrane
z_i	Valence of Solute i

Superscripts

(t)	Iteration t of EM Algorithm
exp	Experimental Measurement
mod	Model Prediction

Subscripts

a, X	Anion
b	Bulk Solution
c, M	Cation
f	Feed Stream
i	Species Index
m	Solution-Membrane Interface
N	Neutral Species
p	Permeate Stream

Fraktur Symbols

$\mathfrak{F}$	Faraday's Constant
$\mathfrak{R}_i^{\mathrm{exp}}$	Experimental Rejection of Solute i
$\mathfrak{R}_i^{\mathrm{lim}}$	Limiting Rejection of Solute i
$\mathfrak{R}_i^{\mathrm{mod}}$	Model Rejection Prediction of Solute i

Appendix A. Pitzer-Kim Multicomponent Activity Model

Short-range and long-range interactions with neighbouring ions and solvent molecules can lead to deviations from ideal behaviour. To incorporate the effect of these non-idealities, activity coefficients, γ_i, of each ion species i, are required. Similarly, for the solvent, an osmotic coefficient, ϕ, is also needed to quantify the deviation from van 't Hoff's law.

Pitzer-Kim's model for mixed electrolyte solutions is a well-established method for quantifying these activity and osmotic coefficients (Pitzer, 1973). The model has previously shown strong agreement with experimental data for many different multicomponent solutions (Pitzer, 1973). The approach is derived by decomposing the solutions' excess Gibbs free energy into a virial expansion that is truncated after the ternary term. For a given cation in solution, the activity coefficient, γ_M, is:

$$\ln\gamma_M = z_M^2\mathrm{F} + \sum_{a=1}^{N_a} m_a(2B_{Ma} + ZC_{Ma}) + \sum_{c=1}^{N_c} m_c(2\phi_{Mc} + \sum_{a=1}^{N_a} m_a\psi_{Mca}) + \sum_{a=1}^{N_a-1}\sum_{a'=a+1}^{N_a} m_a m_{a'}\psi_{aa'M} + |z_M|\sum_{c=1}^{N_c}\sum_{a=1}^{N_a} m_c m_a C_{ca} + \sum_{n=1}^{N_n} m_n(\lambda_{nM}) \quad \text{(A.1)}$$

Similarly, for an anion in solution, the activity coefficient, γ_X, is:

$$\ln\gamma_X = z_X^2\mathrm{F} + \sum_{c=1}^{N_c} m_c(2B_{Xc} + ZC_{Xc}) + \sum_{a=1}^{N_a} m_a(2\phi_{Xa} + \sum_{c=1}^{N_c} m_c\psi_{Xca}) + \sum_{c=1}^{N_c-1}\sum_{c'=c+1}^{N_c} m_c m_{c'}\psi_{cc'X} + |z_X|\sum_{c=1}^{N_c}\sum_{a=1}^{N_a} m_c m_a C_{ca} + \sum_{n=1}^{N_n} m_n(\lambda_{nX}) \quad \text{(A.2)}$$

Lastly, the osmotic coefficient of the solution, ϕ, is given by:

$$\frac{1}{2}\sum_{i=1}^{N_s} m_i(\phi-1) = \frac{-A^\phi\sqrt{I^3}}{1+1.2\sqrt{I}} + \sum_{c=1}^{N_c}\sum_{a=1}^{N_a} m_c m_a(B^\phi_{MX} + ZC_{ca}) + \sum_{c=1}^{N_c-1}\sum_{c'=c+1}^{N_c} m_c m_{c'}(\Phi^\phi_{cc'} + \sum_{a=1}^{N_a} m_a\psi_{cc'a}) + \sum_{a=1}^{N_a-1}\sum_{a'=a+1}^{N_a} m_a m_{a'}(\Phi^\phi_{aa'} + \sum_{c=1}^{N_c} m_c\psi_{aa'c}) + \sum_{n=1}^{N_n}\sum_{a=1}^{N_a} m_n m_a\lambda_{na} + \sum_{n=1}^{N_n}\sum_{c=1}^{N_c} m_n m_c\lambda_{nc} \quad \text{(A.3)}$$

where the subscript s denotes all solutes (including cations, anions, and neutrals). Here, F is depends on ionic strength and can be quantified using:

$$\mathrm{F} = -A^\phi\left[\frac{\sqrt{I}}{1+1.2\sqrt{I}} + \frac{1}{1.2}\ln(1+1.2\sqrt{I})\right] + \sum_{c=1}^{N_c}\sum_{a=1}^{N_a} m_c m_a B'_{ca} + \sum_{c=1}^{N_c-1}\sum_{c'=c+1}^{N_c} m_c m_{c'}\Phi'_{cc'} + \sum_{a=1}^{N_a-1}\sum_{a'=a+1}^{N_a} m_a m_{a'}\Phi'_{aa'} \quad \text{(A.4)}$$

where, A^ϕ is one-third of the Debye limiting gradient (Archer and Wang, 1990)[8]. Using only A^ϕ provides accurate activity and osmotic coefficient predictions at concentrations below 0.8 mol/kg but fails to capture the solution non-idealities at elevated concentrations, requiring additional binary and ternary terms. Subscripts M, X, and N denote cations, anions, and uncharged species, respectively. Similar definitions apply to indices c, a, and n, while N_c, N_a, and N_n correspond to the total number of cations, anions, and uncharged species in solution, respectively. Lastly, z is ion valence and m is the molality of a given species. The remaining terms represent binary and ternary interaction parameters and virial coefficients that can be determined using the expressions below:

$$B^\phi_{MX} = \beta^{(0)}_{MX} + \beta^{(1)}_{MX}e^{-\alpha_{MX}\sqrt{I}} + \beta^{(2)}_{MX}e^{-12\sqrt{I}} \quad \text{(A.5)}$$

$$B_{MX} = \beta^{(0)}_{MX} + \beta^{(1)}_{MX}g(\alpha_{MX}\sqrt{I}) + \beta^{(2)}_{MX}g(12\sqrt{I}) \quad \text{(A.6)}$$

$$B'_{MX} = \beta^{(1)}_{MX}\frac{g'(\alpha_{MX}\sqrt{I})}{I} + \beta^{(2)}_{MX}\frac{g'(12\sqrt{I})}{I} \quad \text{(A.7)}$$

$$C_{MX} = \frac{C^\phi_{MX}}{2|z_M z_X|^{0.5}} \quad \text{(A.8)}$$

Here, I is the solution's ionic strength $\left(\frac{1}{2}\sum_i m_i z_i^2\right)$, and Z is $\sum_i m_i|z_i|$. The parameter C^ϕ_{MX} remains fixed for a given ion pair and values for different pairs are tabulated in literature. Functions $g(\xi)$ and $g'(\xi)$ are:

$$g(\xi) = \left(\frac{2}{\xi^2}\right)\left[1-(1+\xi)e^{-\xi}\right] \quad \text{(A.9)}$$

$$g'(\xi) = -\left(\frac{2}{\xi^2}\right)\left[1-\left(1+\xi+\frac{\xi^2}{2}\right)e^{-\xi}\right] \quad \text{(A.10)}$$

Here, ξ depends on ionic strength and takes the form of $\alpha_{MX}\sqrt{I}$ and/or $12\sqrt{I}$ depending on valence of the ions present in solution. For 2-2 electrolytes and higher non-univalent pairs, $\alpha_{MX} = 1.4$. For simpler pairing (1-1, 1-2, 2-1), a value of 2 is adopted for α_{MX}. Similarly, for 2-2 electrolytes and other high valence pairs, $\beta^{(2)}_{MX}$ is non-zero. $\beta^{(2)}_{MX} = 0$ for univalent ion pairs and other simple ionic pairings e.g. 1-2, 2-1. The second virial coefficient, Φ is a function of ionic strength. Φ is calculated as follows:

$$\Phi^\phi_{ij} = \theta_{ij} + {}^E\theta_{ij}(I) + I{}^E\theta'_{ij}(I) \quad \text{(A.11)}$$

$$\Phi_{ij} = \theta_{ij} + {}^E\theta'_{ij}(I) \quad \text{(A.12)}$$

$$\Phi'_{ij} = {}^E\theta_{ij}(I) \quad \text{(A.13)}$$

[8] A^ϕ is a function of density and temperature. Experimentally-validated pressure, temperature, and salinity-dependent density corrections were applied in this work (Nayar et al., 2016).

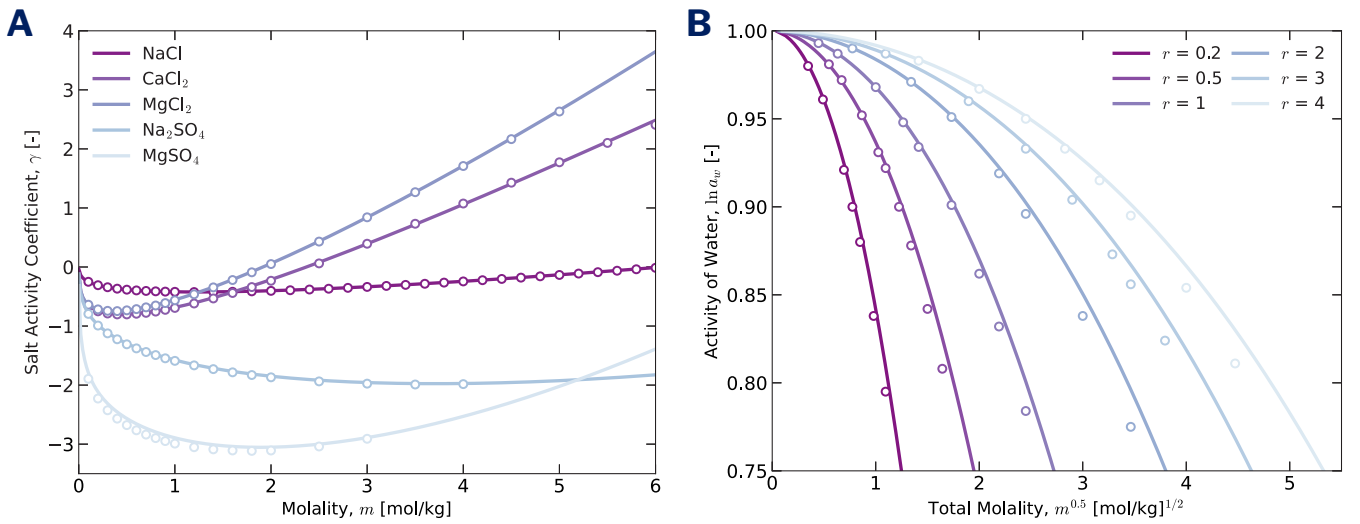

Figure A.6: **(A)** Pitzer-Kim multi-electrolyte model compared to experimental data for various single salts (Robinson and Stokes, 2002). The salts include NaCl, $CaCl_2$, $MgCl_2$, Na_2SO_4, and $MgSO_4$. **(B)** Comparison of model and experiments using the Pitzer-Kim model for multi-electrolyte mixtures of NaCl-KCl with different solute molal ratios denoted by r ($r = 0$ denotes pure KCl and $r \to \infty$ denotes pure NaCl) (Dinane et al., 2002).

${}^{E}\theta_{ij}(I)$ and ${}^{E}\theta'_{ij}(I)$ are function of the solution's ionic strength and a given ion pairing. The corresponding functions are provided by Eq.'s (A.14)-(A.17). Lastly, ${}^{E}\theta_{ij}$ depends on the electrolyte pair and values for each ion pairing are available in the literature.

$$ {}^{E}\theta_{ij}(I) = \frac{z_i z_j}{4I}\left(J_0(x_{ij}) - \frac{1}{2}J_0(x_{ii}) - \frac{1}{2}J_0(x_{jj})\right) \tag{A.14} $$

$$ {}^{E}\theta'_{ij}(I) = \frac{z_i z_j}{8I^2}\left(J_1(x_{ij}) - \frac{1}{2}J_1(x_{ii}) - \frac{1}{2}J_1(x_{jj})\right) - \frac{{}^{E}\theta_{ij}(I)}{I} \tag{A.15} $$

where $J_0(\nu)$ and $J_1(\nu)$ can be evaluated as follows:

$$ J_0(\nu) = \frac{1}{4}\nu - 1 + \frac{1}{\nu}\int_0^\infty \left[1 - e^{-\frac{\nu}{\mu}e^{-\mu}}\right]\mu^2 d\mu \tag{A.16} $$

$$ J_1(\nu) = \frac{1}{4}\nu - 1 + \frac{1}{\nu}\int_0^\infty \left[1 - \left(1 + \frac{\nu}{\mu}e^{-\mu}\right)e^{-\frac{\nu}{\mu}e^{-\mu}}\right]\mu^2 d\mu \tag{A.17} $$

and $\nu_{ij} \triangleq 6 z_i z_j A^\phi \sqrt{I}$. All integrals were evaluated numerically using Gauss-Kronrod quadrature from the `scipy.integrate` package.

Appendix B. EM Algorithm: Proof of Correctness

During the iterative expectation-maximization procedure, it is not directly obvious why maximizing the conditional expectation, $Q(\hat{\theta}|\hat{\theta}^{(t)})$, leads to a direct improvement in the MLE problem with the conventional log likelihood $\ln p(\mathfrak{R}^{\text{exp}}|\hat{\theta})$. To prove this, we can start of by using the laws of conditional probability to express the log likelihood as:

$$ \ln p(\mathfrak{R}^{\text{exp}}|\mathcal{L},\hat{\theta}) = \ln p(\mathfrak{R}^{\text{exp}},\mathcal{L}|\hat{\theta}) - \ln p(\hat{\theta}|\mathfrak{R}^{\text{exp}},\mathcal{L}) \tag{B.1} $$

The total probability can be evaluated for all present terms by taking the expectation and summing (or integrating in the continuous case) through all possible latent variables under the current estimate of the pore size parameterization, $\hat{\theta}^{(t)}$:

$$ \ln p(\mathfrak{R}^{\text{exp}}|\hat{\theta}) = \sum_{\mathcal{L}} p(\mathcal{L}|\mathfrak{R}^{\text{exp}},\hat{\theta}^{(t)}) \ln p(\mathfrak{R}^{\text{exp}},\mathcal{L}|\hat{\theta}) - \sum_{\mathcal{L}} p(\mathcal{L}|\mathfrak{R}^{\text{exp}},\hat{\theta}^{(t)}) \ln p(\mathcal{L}|\mathfrak{R}^{\text{exp}},\hat{\theta}) \tag{B.2} $$

Here, the first term on the right-hand-side has been previously defined as $Q(\hat{\theta}|\hat{\theta}^{(t)})$, while the second term can be defined as $\Gamma(\hat{\theta}|\hat{\theta}^{(t)})$:

$$ \ln p(\mathfrak{R}^{\text{exp}}|\hat{\theta}) = Q(\hat{\theta}|\hat{\theta}^{(t)}) + \Gamma(\hat{\theta}|\hat{\theta}^{(t)}) \tag{B.3} $$

Since this equation holds for all iterations of the EM algorithm, the equality must also hold for the current iteration:

$$ \ln p(\mathfrak{R}^{\text{exp}}|\hat{\theta}^{(t)}) = Q(\hat{\theta}^{(t)}|\hat{\theta}^{(t)}) + \Gamma(\hat{\theta}^{(t)}|\hat{\theta}^{(t)}) \tag{B.4} $$

Next, we can evaluate the difference between Eq. (B.3) and Eq. (B.4), denoted Δ, to yield:

$$ \Delta = \left[Q(\hat{\theta}|\hat{\theta}^{(t)}) - Q(\hat{\theta}^{(t)}|\hat{\theta}^{(t)})\right] + \left[\Gamma(\hat{\theta}|\hat{\theta}^{(t)}) - \Gamma(\hat{\theta}^{(t)}|\hat{\theta}^{(t)})\right] \tag{B.5} $$

Here, we can apply Gibbs inequality, which states that for two discrete probability distributions, $\mathcal{P}$ and $\mathcal{Q}$, the following inequality must hold:

$$ -\sum_{i=1}^{N} p_i \ln p_i \leq -\sum_{i=1}^{N} p_i \ln q_i \tag{B.6} $$

where the equality constraint is met if and only if $p_i = q_i \ \forall i$. This inequality arises from information theory arguments which explicitly state that the information entropy of a given distribution $\mathcal{P}$ must be less than or equal to its cross entropy with any other distribution $\mathcal{Q}$.

Consequently, using the Gibbs inequality, $\Gamma(\hat{\theta}|\hat{\theta}^{(t)}) \geq \Gamma(\hat{\theta}^{(t)}|\hat{\theta}^{(t)})$. This means that:

$$ \ln p(\mathfrak{R}^{\text{exp}}|\hat{\theta}) - \ln p(\mathfrak{R}^{\text{exp}}|\hat{\theta}^{(t)}) \geq Q(\hat{\theta}|\hat{\theta}^{(t)}) - Q(\hat{\theta}^{(t)}|\hat{\theta}^{(t)}) \tag{B.7} $$

This proves two things: (**1**) $Q(\hat{\theta}|\hat{\theta}^{(t)})$ must be bounded from above by $\ln p(\mathfrak{R}^{\text{exp}}|\hat{\theta})$; and (**2**) by maximizing $Q(\hat{\theta}|\hat{\theta}^{(t)})$, the optimization achieves at least an equal improvement in the subsequent $\hat{\theta}$ as it would in the case the optimization was performed on $\ln p(\mathfrak{R}^{\text{exp}}|\hat{\theta})$.

This result is presented graphically in Fig. B.7, where a sample curve for $\ln p(\mathfrak{R}^{\text{exp}}|\hat{\theta})$ is provided. Similarly, a qualitative example of $Q(\hat{\theta}|\hat{\theta}^{(t)})$ is plotted, where it is seen to be bounded from above by $\ln p(\mathfrak{R}^{\text{exp}}|\hat{\theta})$, as enforced by the EM algorithm. The next iteration, $\hat{\theta}^{(t+1)}$ is determined by maximizing $Q(\hat{\theta}|\hat{\theta}^{(t)})$. In our case, the Nelder-Mead gradient-free local optimizer is used to evaluate $\hat{\theta}^{(t+1)}$ repeatedly until $|(\hat{\theta}^{(t+1)} - \hat{\theta}^{(t)})/\hat{\theta}^{(t)}| < \varepsilon$, for $\varepsilon = 1 \times 10^{-4}$.

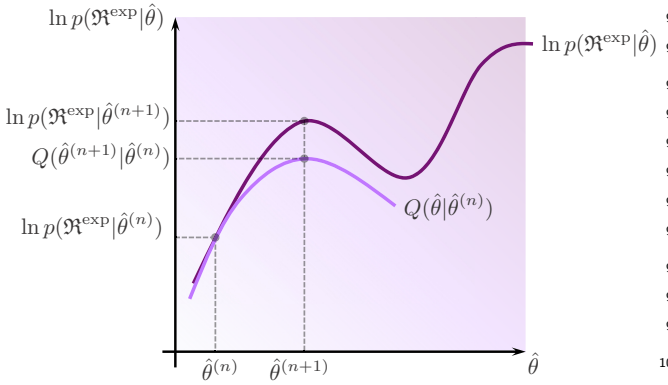

Figure B.7: Qualitative illustration of update procedure for the expectation-maximization algorithm for a given set of latent membrane parameters.

Appendix C. Model Assumptions and Limitations

The conventional DSPM-DE model contains many underlying assumptions and simplifications that have been rigorously detailed in prior work (Wang and Lin, 2021; Yaroshchuk et al., 2019). In this study, we have eliminated some of them to provide better generalizability; however, some simplifications and model limitations remain. Some of the main remaining assumptions/limitations are summarized below (in no particular order):

1. Salts are assumed to fully dissociate in water without forming ion complexes. At brackish salinities, this assumption may be justified, but beyond seawater salinities, the errors that result from this assumption can become substantial (Foo et al., 2023).
2. Charged species transport is explicitly uncoupled (the extended Nernst-Planck equations do not include cross-interaction terms), yet implicitly coupled through the electric potential and electroneutrality constraints imposed on the model formulation. The introduced errors can become substantial in the high salinity regime (Foo et al., 2021; Rehman et al., 2021).
3. The convective and diffusive hindrance factors used to describe transmembrane transport are derived from perturbation theory solutions to the Navier-Stokes equations and treat ions as hard neutral spheres in neutral cylindrical pores (Deen, 1987).
4. The geometric distribution used to describe the steric exclusion partition coefficient was originally derived for cylindrical pores (an alternate formulation for slit-like pores exists, and can be used, however, both are simplifications of the underlying pore morphology) (Yaroshchuk, 2000).
5. The volumetric charge density is assumed to be a homogenous quantity, despite recent literature suggesting a heterogenous, composition-dependent structure (Ritt et al., 2020). A similar argument applies to the dielectric constant inside the polyamide membrane pores.
6. The Born formula used for dielectric exclusion arises from macroscopic electrostatics, which treat the ions as conducting non-polarizable spheres with charges distributed across the ion surface. In addition, the solvent is modelled as a dielectric continuum without structure. This formulation assumes that the induced charges from dielectric effects are distributed locally across an infinitely thin film at the ion-solvent interface, despite dielectric effects most likely arising from a supramolecular structure (Yaroshchuk et al., 2019). A more rigorous discussion around the shortcomings of the Born model is detailed in the review by Yaroshchuk et al. (Yaroshchuk et al., 2019).
7. The framework for image forces linearizes the equations of macroscopic electrostatics, neglecting the importance of water structure under nano-confinement (Yaroshchuk et al., 2019). These effects can lead to reduced ion screening effects of image forces, which may suggest underestimated contributions of image charges in polyamide membranes.
8. Combing steric and Donnan exclusion using partitioning laws can lead to pronounced negative rejections that may disagree with experimental observations (Yaroshchuk et al., 2019).
9. The electroneutrality condition is assumed to hold inside the membrane pores as well as within the bulk solution (Yaroshchuk et al., 2019).
10. The Stokes radius is the most representative radius to use. Previous studies have explored cavity radii, ionic radii, Born radii, and Pauling radii, with varying degrees of success (Hussain et al., 2008).

Appendix D. Classical Characterization Procedure

Here, we summarize the conventional characterization procedure used to determine the four governing latent membrane parameters in NF systems: $\mathcal{L} = \{r_p, \Delta x_e, \zeta_p, \chi_d\}$.

First, uncharged/neutral solute experiments are used to quantify the pore radius, r_p. Solute j's hindered flux in the selective layer when convection and diffusion are the sole driving forces for transport is:

$$J_j = -H_{j,d} D_j \frac{dC_j}{dx} + H_{j,c} J_v C_j \tag{D.1}$$

where $H_{j,d}$ and $H_{j,c}$ are diffusive and convective hindrance coefficients that include steric corrections, respectively. By integrating both sides of the equation, we obtain:

$$\int_{C_{j,f}}^{C_{j,p}} \frac{1}{H_{j,c} J_v C_j - J_j} dC_j = \int_0^{\Delta x_e} \frac{1}{H_{j,d} D_j} dx \tag{D.2}$$

The integral is performed from the feed to the permeate, under the assumption that the concentrations are sufficiently low enough for insignificant boundary layer formation. This can often be achieved by high cross-flow velocities that minimize concentration polarization (Bowen et al., 1997; Schaep et al., 1999). Performing the integral and substituting in the limits yields:

$$\ln\left(\frac{H_{j,c} J_v C_{j,p} - J_j}{H_{j,c} J_v C_{j,f} - J_j}\right) = \frac{H_{j,c} J_v \Delta x_e}{H_{j,d} D_j} \tag{D.3}$$

where the right-hand-side corresponds to the Péclet number (the ratio of convective transport to diffusive transport):

$$\text{Pe}_j \triangleq \frac{H_{j,c} J_v \Delta x_e}{H_{j,d} D_j} \tag{D.4}$$

Exponentiating both sides of Eq. (D.3) and assuming a decoupled solute and solvent flux, we obtain:

$$\frac{J_j(1-H_{j,c})}{J_j - H_{j,c}J_v C_{j,f}} = \exp\left(\mathrm{Pe}_j\right) \tag{D.5}$$

Rearranging Eq. (D.5) for J_j yields:

$$J_j = \frac{H_{j,c}J_v C_{j,f}}{1-\left(1-H_{j,c}\right)\exp\left(-\mathrm{Pe}_j\right)} \tag{D.6}$$

Since $H_{j,c} \triangleq K_{j,c}(1-\lambda_j)^2$ and $H_{j,d} \triangleq K_{j,d}(1-\lambda_j)^2$, we can re-write Eq. (D.6) as:

$$J_j = \frac{K_{j,c}(1-\lambda_j)^2 J_v C_{j,f}}{1-\left[1-K_{j,c}\left(1-\lambda_j\right)^2\right]\exp\left(-\mathrm{Pe}_j\right)} \tag{D.7}$$

Finally, both sides are divided by $J_v C_{j,f}$, and we replace J_j with $J_v C_{j,p}$, while subtracting the equation from 1 to obtain uncharged solute rejection, $\mathfrak{R}_j^{\mathrm{mod}}$:

$$\mathfrak{R}_j^{\mathrm{mod}} \triangleq 1 - \frac{C_{j,p}}{C_{j,f}} = 1 - \frac{K_{j,c}(1-\lambda_j)^2}{1-\left[1-K_{j,c}\left(1-\lambda_j\right)^2\right]\exp\left(-\mathrm{Pe}_j\right)} \tag{D.8}$$

This equation characterizes uncharged solute rejection under the assumption that no boundary layers exist in the feed or the permeate. Next, substituting the Hagen-Poiseuille relation into Pe_j, the rejection becomes entirely a function of r_p, removing the dependence on the effective membrane thickness i.e. $\mathfrak{R}_j^{\mathrm{mod}}(r_p, \Delta x_e) \rightarrow \mathfrak{R}_j^{\mathrm{mod}}(r_p)$:

$$\mathrm{Pe}_j(r_p, \Delta x_e) = \frac{H_{j,c}\Delta x_e}{H_{j,d}D_j} \cdot \underbrace{\frac{r_p^2 \Delta P}{8\mu_w \Delta x_e}}_{J_v} = \frac{H_{j,c}r_p^2 \Delta P}{8\mu H_{j,d} D_j} = \mathrm{Pe}_j(r_p) \tag{D.9}$$

Here, μ_w is the solution dynamic viscosity and the Hagen-Poiseuille equation is substituted in for J_v. The Hagen-Poiseuille equation is derived under the assumption of fully-developed laminar flow in straight cylindrical tubes, which may be a significant simplification of the underlying physics. This substitution simultaneously introduces, ΔP, the applied pressure, an easy-to-measure independent parameter. Some studies in the literature substitute ΔP with ΔP_{eff}, which purports to account for the osmotic pressure difference between the feed and permeate (Wang and Lin, 2021; Bandini and Vezzani, 2003).

In some studies, instead of using $\mathfrak{R}_j^{\mathrm{mod}}$ from Eq. (D.8), authors replace it with the rejection in the high Péclet number regime, $\mathfrak{R}_j^{\mathrm{lim}}$. Here, as $\mathrm{Pe}_j \rightarrow \infty$, $\mathfrak{R}_j^{\mathrm{mod}} \rightarrow \mathfrak{R}_j^{\mathrm{lim}}$, where $\mathfrak{R}_j^{\mathrm{lim}} = 1 - K_{j,c}\left(1-\lambda_j\right)^2$ (Labban et al., 2017). This value is often termed the limiting rejection.

Using the rejection formulation from Eq. (D.8), a one dimensional least squares regression can be performed to fit the pore radius. The optimization problem takes the following form:

$$r_p^* = \underset{r_p}{\mathrm{argmin}} \sum_{i=1}^{N_v}\sum_{j=1}^{N_{\mathbb{U}}}\left[\mathfrak{R}_{i,j}^{\mathrm{mod}}(r_p) - \mathfrak{R}_{i,j}^{\mathrm{exp}}\right]^2 \tag{D.10}$$

Here, indices i and j run through all water flux measurements and uncharged solutes, respectively. $N_{\mathbb{U}}$ corresponds to the total number of uncharged species in solution. All latent variables with an asterisk in the subscript denote optimal values.

Once the pore radius has been determined from uncharged species rejection data, its value is substituted back into the Hagen-Poiseuille equation to regress out membrane thickness by fitting J_v to applied pressure. Most frequently, pure water permeability studies are used to perform this regression, with the optimization problem formulated in Eq. (D.11) below (Micari et al., 2020):

$$\Delta x_e^* = \underset{\Delta x_e}{\mathrm{argmin}} \sum_{i=1}^{N_v}\left[\frac{r_p^2 \Delta P_i}{8\mu_w \Delta x_e} - J_{v,i}^{\mathrm{exp}}\right]^2 \tag{D.11}$$

Some variations to this approach do exist in the literature. Authors have also previously combined the single-variable minimization into a simultaneous regression for both water flux and uncharged species rejection (Wang et al., 2021b). This leads to the following optimization problem:

$$\begin{aligned}(r_p^*, \Delta x_e^*) = \underset{r_p,\, \Delta x_e}{\mathrm{argmin}} & \sum_{i=1}^{N_v}\left[\frac{J_{v,i}^{\mathrm{mod}}(r_p,\, \Delta x_e) - J_{v,i}^{\mathrm{exp}}}{J_{v,i}^{\mathrm{exp}}}\right]^2 \\ & + \sum_{i=1}^{N_v}\sum_{j=1}^{N_{\mathbb{U}}}\left[\frac{\mathfrak{R}_{i,j}^{\mathrm{mod}}(r_p,\, \Delta x_e) - \mathfrak{R}_{i,j}^{\mathrm{exp}}}{\mathfrak{R}_{i,j}^{\mathrm{exp}}}\right]^2\end{aligned} \tag{D.12}$$

Although this approach allows both r_p and Δx_e to vary simultaneously, an explicit water flux equation is still required for its use.

Now that the pore radius, r_p, and the effective thickness, Δx_e, have been quantified, two latent variables remain: ζ_p and χ_d. The next parameter determined is the dielectric constant in the membrane pores, ζ_p. To evaluate this, zeta potential measurements are first performed to determine the iso-electric point (IEP) of the membranes. At this point, the membrane is deemed to be neutrally-charged, suggesting that Donnan effects can be ignored. Mathematically, under these conditions, $\chi_d = 0$. Under these operating conditions, the dimensionality of the regression problem is reduced. Now, with the neutrally-charged membrane, single salt rejection experiments can be performed and used as inputs in the following optimization problem (holding the previously determined values of r_p and Δx_e constant):

$$\zeta_p^* = \underset{\zeta_p}{\mathrm{argmin}} \sum_{i=1}^{N_v}\left[\mathfrak{R}_i^{\mathrm{mod}}(r_p,\, \Delta x_e,\, \zeta_p,\, \chi_d = 0) - \mathfrak{R}_i^{\mathrm{exp}}\right]^2 \tag{D.13}$$

Here, $\mathfrak{R}_i^{\mathrm{mod}}$ is now determined using the full DSPM-DE model (with χ_d set to 0). After using this regression to quantify ζ_p, the last remaining latent variable is the volumetric membrane charge density, χ_d (since $\chi_d \neq 0$ at values other than the IEP). To evaluate χ_d, multicomponent rejection measurements can be performed at pH 7. The full DSPM-DE model is used to determine multicomponent rejection as a function of permeate water flux or applied pressure. This rejection serves as input into the objective function that minimizes the least squares error between the model output and experimental data:

$$\chi_d^* = \underset{\chi_d}{\mathrm{argmin}} \sum_{i=1}^{N_v}\sum_{j=1}^{N_{\mathbb{S}}}\left[\mathfrak{R}_{i,j}^{\mathrm{mod}}(r_p,\, \Delta x_e,\, \zeta_p,\, \chi_d) - \mathfrak{R}_{i,j}^{\mathrm{exp}}\right]^2 \tag{D.14}$$

Here, $N_{\mathbb{S}}$ denotes the total number of ions in solution.

To summarize the conventional characterization procedure, a schematic of the process is provided in Fig. D.8 below.

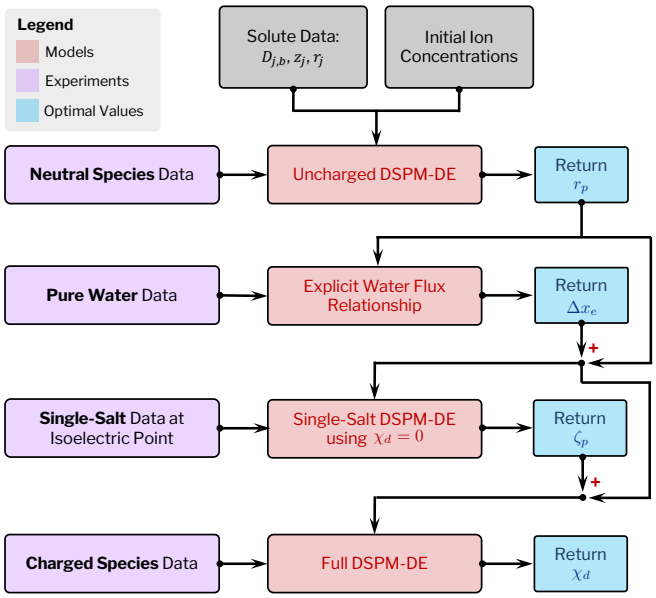

Figure D.8: Conventional characterization procedure for determining the four latent membrane parameters from experimental data. Four sets of experiments are needed: (**1**) uncharged solute rejection experiments to derive pore radius; (**2**) pure water flux experiments at varying operating pressures to quantify the effective membrane thickness; (**3**) single salt rejection measurements at the membrane's IEP (χ_d is assumed to be 0); and (**4**) multicomponent rejection experiments to quantify the membrane charge density (Rehman and Lienhard, 2022).

Appendix E. Ultraspherical Spectral Methods for Accelerated Numerical Computation

When discretizing the extended Nernst-Planck equations from Eq. (1), an equally-spaced collocation grid is most often used; however, switching to a Chebyshev discretization grid and adopting ultraspherical spectral methods – a relatively new numerical approach to solving linear systems – can provide substantial computational benefits (Olver and Townsend, 2013). Specifically, the numerical solution procedure shifts from requiring $\mathcal{O}(N^3)$ operations for matrix inversion to $\mathcal{O}(N \log N)$ operations. These runtimes, $\mathcal{O}(\cdot)$, correspond to asymptotic complexities, where N refers to the number of the points used in the discretization (Olver and Townsend, 2013).

Spectral methods in collocation space are typically dense linear operators that yield exponential convergence rates for linear systems (this also holds true for spectral Chebyshev operators on the collocation grid) (Trefethen, 2000). Although spectral accuracy is achieved, this comes at the expense of $\mathcal{O}(N^3)$ inversion. Low-order finite difference methods on the other hand, require $\mathcal{O}(N)$ operations to invert (assuming the matrix bandwidth is not a function of the discretization size), yet suffer from polynomial convergence rates. Ultraspherical spectral methods adopt discrete cosine transforms (DCTs) to perform fast mappings between points on the collocation grid to a new coefficient space, where the previously dense differential operators become sparse, banded matrices. The primary advantage is that these preconditioner mappings can be computed quickly, i.e. in $\mathcal{O}(N \log N)$ operations, after which we can resort back to our fast $\mathcal{O}(N)$ inversion algorithms in this new coefficient space. Once the new linear system has been inverted, the resultant solution is mapped back onto the collocation grid using inverse DCTs, also at $\mathcal{O}(N \log N)$. This yields an overall asymptotic complexity of $\mathcal{O}(N \log N)$ for spectral accuracy, which is substantially faster than an $\mathcal{O}(N^3)$ complexity, which would be needed if the system were solved on collocation points. Note: DCTs are used in the case where Dirichlet boundary conditions define the problem PDE, which is the case for the DSPM-DE model and our approach. If periodic boundary conditions are present, fast Fourier transforms (FFTs) can be used, and in the case of Neumann boundary conditions, discrete sine transforms (DSTs) can be adopted. The choice of preconditioner is essential in determining whether the resultant matrix in coefficient space is banded or not; an attribute that we desire in order to leverage the fast $\mathcal{O}(N)$ inversions.

When combining these numerical methods with our model, the degree of discretization needed to achieve the same solution accuracy is substantially lower: specifically, we are able to achieve machine precision numerical accuracy in the selective layer concentration with only 10 discretization nodes, reducing the amount of computation required from the numerical scheme (Geraldes and Afonso, 2007).

The Chebyshev grid is a projection of a uniformly-spaced grid on the surface of a semi-circle onto the Cartesian plane (see Fig. E.9; here, the equally-spaced nodes on the semi-circle, separated by Δx, are projected onto the horizontal axis, creating an unequally-spaced grid at Chebyshev nodes). There is a higher density of nodes near the solution-membrane interface (at $x = 0^-/0^+$ and $x = \Delta x_e^-/\Delta x_e^+$) and a lower density at the center of the selective layer.

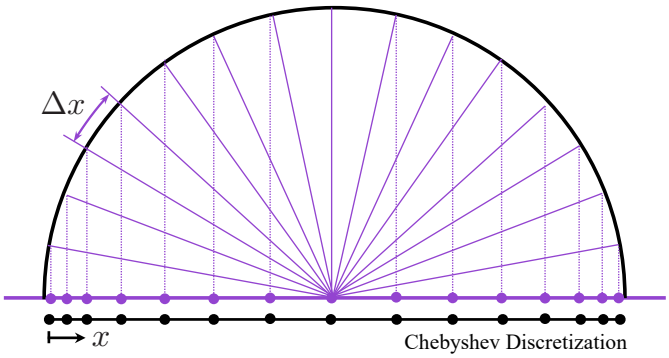

Figure E.9: Chebyshev discretization visualization; projection from equally-spaced grid on the semi-circle to unequally-spaced points on a Cartesian plane.

In collocation space, the Chebyshev spectral derivative operators (Trefethen, 2000) are:

$$\mathcal{D}_\lambda = \begin{cases} (2\lambda^2+1)/6 & i,j = 0 \\ -(2\lambda^2+1)/6 & i,j = \lambda \\ -0.5x_j(1-x_j^2)^{-1} & 1 < i = j \leq \lambda - 1 \\ (d_i/d_j)(-1)^{i+j}(x_i - x_j)^{-1} & 1 < i \neq j \leq \lambda - 1 \end{cases} \tag{E.1}$$

where λ is the order of differentiation and d_i is defined as:

$$d_i = \begin{cases} 2 & i = 0 \text{ or } \lambda \\ 1 & 1 \leq i \leq \lambda - 1 \end{cases} \tag{E.2}$$

In coefficient space, these operators become banded matrices, $\tilde{\mathcal{D}}_\lambda$:

$$\tilde{\mathcal{D}}_\lambda = \begin{cases} \lambda + i & j = \lambda + i \\ 0 & \text{elsewhere} \end{cases} \tag{E.3}$$

References

Claudia W. Sadoff, Edoardo Borgomeo, and Stefan Uhlenbrook. Rethinking Water for SDG 6. *Nature Sustainability*, 3(5):346–347, 2020. doi: 10.1038/s41893-020-0530-9. URL https://doi.org/10.1038/s41893-020-0530-9.

Ryan M. DuChanois, Mohammad Heiranian, Jason Yang, Cassandra J. Porter, Qilin Li, Xuan Zhang, Rafael Verduzco, and Menachem Elimelech. Designing polymeric membranes with coordination chemistry for high-precision ion separations. *Science Advances*, 8(9):eabm9436, 2022. URL https://doi.org/10.1126/sciadv.abm9436.

Benjamin K. Sovacool, Saleem H. Ali, Morgan Bazilian, Ben Radley, Benoit Nemery, Julia Okatz, and Dustin Mulvaney. Sustainable minerals and metals for a low-carbon future. *Science*, 367(6473):30–33, 2020. URL https://doi.org/10.1126/science.aaz6003.

Alexander S. Ivanov, Christina J. Leggett, Bernard F. Parker, Zhicheng Zhang, John Arnold, Sheng Dai, Carter W. Abney, Vyacheslav S. Bryantsev, and Linfeng Rao. Origin of the unusually strong and selective binding of vanadium by polyamidoximes in seawater. *Nature Communications*, 8(1):1560, 2017. URL https://doi.org/10.1038/s41467-017-01443-1.

Ryan M. DuChanois, Nathanial J. Cooper, Boreum Lee, Sohum K. Patel, Lauren Mazurowski, Thomas E. Graedel, and Menachem Elimelech. Prospects of metal recovery from wastewater and brine. *Nature Water*, 1(1):37–46, 2023. URL https://doi.org/10.1038/s44221-022-00006-z.

Prashant S. Kulkarni. Recovery of Uranium(VI) from acidic wastes using tri-n-octylphosphine oxide and sodium carbonate based liquid membranes. *Chemical Engineering Journal*, 92(1):209–214, 2003. URL https://doi.org/10.1016/S1385-8947(02)00255-3.

Tonni Agustiono Kurniawan, Gilbert Y.S. Chan, Wai-Hung Lo, and Sandhya Babel. Physico–chemical treatment techniques for wastewater laden with heavy metals. *Chemical Engineering Journal*, 118(1):83–98, 2006. URL https://doi.org/10.1016/j.cej.2006.01.015.

Amir Razmjou, Mohsen Asadnia, Ehsan Hosseini, Asghar Habibnejad Korayem, and Vicki Chen. Design principles of ion selective nanostructured membranes for the extraction of lithium ions. *Nature Communications*, 10(1):5793, 2019. URL https://doi.org/10.1038/s41467-019-13648-7.

Sharaniya Roobavannan, Saravanamuthu Vigneswaran, and Gayathri Naidu. Enhancing the performance of membrane distillation and ion-exchange manganese oxide for recovery of water and lithium from seawater. *Chemical Engineering Journal*, 396:125386, 2020. URL https://doi.org/10.1016/j.cej.2020.125386.

Jan-Max Arana Juve, Frederick Munk S. Christensen, Yong Wang, and Zongsu Wei. Electrodialysis for metal removal and recovery: A review. *Chemical Engineering Journal*, 435:134857, 2022. URL https://doi.org/10.1016/j.cej.2022.134857.

Yvana D. Ahdab, Georg Schücking, Danyal Rehman, and John H. Lienhard. Cost effectiveness of conventionally and solar powered monovalent selective electrodialysis for seawater desalination in greenhouses. *Applied Energy*, 301:117425, 2021. URL https://doi.org/10.1016/j.apenergy.2021.117425.

Razi Epsztein, Oded Nir, Ori Lahav, and Michal Green. Selective nitrate removal from groundwater using a hybrid nanofiltration–reverse osmosis filtration scheme. *Chemical Engineering Journal*, 279:372–378, 2015. URL https://doi.org/10.1016/j.cej.2015.05.010.

Razi Epsztein, Ryan M. DuChanois, Cody L. Ritt, Aleksandr Noy, and Menachem Elimelech. Towards single-species selectivity of membranes with subnanometre pores. *Nature Nanotechnology*, 15(6):426–436, 2020. doi: 10.1038/s41565-020-0713-6. URL https://doi.org/10.1038/s41565-020-0713-6.

Andrea Schäfer, Anthony G. Fane, and T. David Waite. *Nanofiltration: Principles, Applications, and New Materials*. Elsevier, 2005.

Ahmad Rahimpour, Mohsen Jahanshahi, Narmin Mortazavian, Sayed Siavash Madaeni, and Yaghob Mansourpanah. Preparation and characterization of asymmetric polyethersulfone and thin-film composite polyamide nanofiltration membranes for water softening. *Applied Surface Science*, 256(6):1657–1663, 2010. URL https://doi.org/10.1016/j.apsusc.2009.09.089.

Patrizia Marchetti, Maria F. Jimenez Solomon, Gyorgy Szekely, and Andrew G. Livingston. Molecular separation with organic solvent nanofiltration: A critical review. *Chemical Reviews*, 114(21):10735–10806, 2014. URL https://doi.org/10.1021/cr500006j.

Panchakshari Z. V. Murthy and Latesh B. Chaudhari. Separation of binary heavy metals from aqueous solutions by nanofiltration and characterization of the membrane using spiegler–kedem model. *Chemical Engineering Journal*, 150(1):181–187, 2009. URL https://doi.org/10.1016/j.cej.2008.12.023.

Varun H. Hegde, Michael F. Doherty, and Todd M. Squires. A two-phase model that unifies and extends the classical models of membrane transport. *Science*, 377(6602):186–191, 2022. URL https://doi.org/10.1126/science.abm7192.

Ora Kedem and Aharon Katchalsky. Permeability of composite membranes. part 1.—electric current, volume flow and flow of solute through membranes. *Transactions of the Faraday Society*, 59:1918–1930, 1963. URL http://dx.doi.org/10.1039/TF9635901918.

Kurt S. Spiegler and Ora Kedem. Thermodynamics of hyperfiltration (reverse osmosis): criteria for efficient membranes. *Desalination*, 1(4):311–326, 1966. URL https://doi.org/10.1016/S0011-9164(00)80018-1.

Mordechai Perry and Charles Linder. Intermediate reverse osmosis ultrafiltration (ro uf) membranes for concentration and desalting of low molecular weight organic solutes. *Desalination*, 71(3):233–245, 1989. URL https://doi.org/10.1016/0011-9164(89)85026-X.

William M. Deen. Hindered transport of large molecules in liquid-filled pores. *AIChE Journal*, 33(9):1409–1425, 1987. URL https://doi.org/10.1002/aic.690330902.

W. Richard Bowen and Hilmi Mukhtar. Characterisation and prediction of separation performance of nanofiltration membranes. *Journal of Membrane Science*, 112(2):263–274, 1996. URL https://doi.org/10.1016/0376-7388(95)00302-9.

W. Richard Bowen and Abdul Wahab Mohammad. Diafiltration by nanofiltration: Prediction and optimization. *AIChE Journal*, 44(8):1799–1812, 1998. URL https://doi.org/10.1002/aic.690440811.

W. Richard Bowen and Julian S. Welfoot. Modelling the performance of membrane nanofiltration—critical assessment and model development. *Chemical Engineering Science*, 57(7):1121–1137, 2002a. URL https://doi.org/10.1016/S0009-2509(01)00413-4.

Timothy T. Duignan and Xiu S. Zhao. The Born model can accurately describe electrostatic ion solvation. *Physical Chemistry Chemical Physics*, 22:25126–25135, 2020. URL http://dx.doi.org/10.1039/D0CP04148C.

Nidal Hilal, Habis Al-Zoubi, Naif A. Darwish, and Abdul Wahab Mohammad. Characterisation of nanofiltration membranes using atomic force microscopy. *Desalination*, 177(1):187–199, 2005. URL https://doi.org/10.1016/j.desal.2004.12.008.

W. Richard Bowen, Abdul Wahab Mohammad, and Nidal Hilal. Characterisation of nanofiltration membranes for predictive purposes — use of salts, uncharged solutes and atomic force microscopy. *Journal of Membrane Science*, 126(1):91–105, 1997. URL https://doi.org/10.1016/S0376-7388(96)00276-1.

W. Richard Bowen and Julian S. Welfoot. Modelling of membrane nanofiltration—pore size distribution effects. *Chemical Engineering Science*, 57(8):1393–1407, 2002b. URL https://doi.org/10.1016/S0009-2509(01)00412-2.

Xiao Wang, Dufei Fang, Benjamin S. Hsiao, and Benjamin Chu. Nanofiltration membranes based on thin-film nanofibrous composites. *Journal of Membrane Science*, 469:188–197, 2014. URL https://doi.org/10.1016/j.memsci.2014.06.049.

Sushuang Li, Jianquan Luo, Xiaofeng Hang, Shiguang Zhao, and Yinhua Wan. Removal of polycyclic aromatic hydrocarbons by nanofiltration membranes: Rejection and fouling mechanisms. *Journal of Membrane Science*, 582:264–273, 2019. URL https://doi.org/10.1016/j.memsci.2019.04.008.

Qingyuan He, Yifei Hu, Xingzheng Li, Meihong Liu, Sanchuan Yu, and Congjie Gao. Pore size regulation of polyamide composite membrane via a sol-gel process confined within the selective layer. *Journal of Membrane Science*, 655:120581, 2022. URL https://doi.org/10.1016/j.memsci.2022.120581.

Ruoyu Wang and Shihong Lin. Pore model for nanofiltration: History, theoretical framework, key predictions, limitations, and prospects. *Journal of Membrane Science*, 620:118809, 2021. URL https://doi.org/10.1016/j.memsci.2020.118809.

Victor M. Starov and Nikolai V. Churaev. Separation of electrolyte solutions by reverse osmosis. *Advances in Colloid and Interface Science*, 43(2):145–167, 1993. URL https://doi.org/10.1016/0001-8686(93)80016-5.

Anthony Szymczyk and Patrick Fievet. Investigating transport properties of

nanofiltration membranes by means of a steric, electric and dielectric exclusion model. *Journal of Membrane Science*, 252(1):77–88, 2005. URL https://doi.org/10.1016/j.memsci.2004.12.002.

Bouranene Saliha, Fievet Patrick, and Szymczyk Anthony. Investigating nanofiltration of multi-ionic solutions using the steric, electric and dielectric exclusion model. *Chemical Engineering Science*, 64(17):3789–3798, 2009. URL https://doi.org/10.1016/j.ces.2009.05.020.

Altaf A. Hussain, Mohamed E. E. Abashar, and Ibrahim S. Al-Mutaz. Influence of ion size on the prediction of nanofiltration membrane systems. *Desalination*, 214(1):150–166, 2007. URL https://doi.org/10.1016/j.desal.2006.10.022.

Altaf A. Hussain, Sanna K. Nataraj, Mohamed E. E. Abashar, Ibrahim S. Al-Mutaz, and Tejraj M. Aminabhavi. Prediction of physical properties of nanofiltration membranes using experiment and theoretical models. *Journal of Membrane Science*, 310(1):321–336, 2008. URL https://doi.org/10.1016/j.memsci.2007.11.005.

Serena Bandini and Daniele Vezzani. Nanofiltration modeling: the role of dielectric exclusion in membrane characterization. *Chemical Engineering Science*, 58(15):3303–3326, 2003. URL https://doi.org/10.1016/S0009-2509(03)00212-4.

Andriy E. Yaroshchuk. Dielectric exclusion of ions from membranes. *Advances in Colloid and Interface Science*, 85(2):193–230, 2000. URL https://doi.org/10.1016/S0001-8686(99)00021-4.

Andriy E. Yaroshchuk. Non-steric mechanisms of nanofiltration: superposition of donnan and dielectric exclusion. *Separation and Purification Technology*, 22-23:143–158, 2001. URL https://doi.org/10.1016/S1383-5866(00)00159-3.

Darren L. Oatley, Laia Llenas, Ramon Pérez, Paul M. Williams, Xavier Martínez-Lladó, and Miquel Rovira. Review of the dielectric properties of nanofiltration membranes and verification of the single oriented layer approximation. *Advances in Colloid and Interface Science*, 173:1–11, 2012. URL https://doi.org/10.1016/j.cis.2012.02.001.

Sébastien Déon, Aurélie Escoda, and Patrick Fievet. A transport model considering charge adsorption inside pores to describe salts rejection by nanofiltration membranes. *Chemical Engineering Science*, 66(12):2823–2832, 2011. URL https://doi.org/10.1016/j.ces.2011.03.043.

Béatrice Balannec, Aziz Ghoufi, and Anthony Szymczyk. Nanofiltration performance of conical and hourglass nanopores. *Journal of Membrane Science*, 552:336–340, 2018. URL https://doi.org/10.1016/j.memsci.2018.02.026.

Cody L. Ritt, Jay R. Werber, Mengyi Wang, Zhongyue Yang, Yumeng Zhao, Heather J. Kulik, and Menachem Elimelech. Ionization behavior of nanoporous polyamide membranes. *Proceedings of the National Academy of Sciences*, 117(48):30191–30200, 2020. doi: 10.1073/pnas.2008421117. URL https://doi.org/10.1073/pnas.2008421117.

Danyal Rehman and John H. Lienhard. Global optimization for accurate and efficient parameter estimation in nanofiltration. *Journal of Membrane Science Letters*, 2(2):100034, 2022. URL https://doi.org/10.1016/j.memlet.2022.100034.

Mohamed A. Kammoun, Sana Gassara, John Palmeri, Ben Amar, and André Deratani. Nanofiltration performance prediction for brackish water desalination: case study of Tunisian groundwater. *Desalination and Water Treatment*, 181:27–39, Mar 2020. URL https://dx.doi.org/10.5004/dwt.2020.25100.

Danyal Rehman and John H. Lienhard. Physics-constrained neural differential equations for learning multi-ionic transport. *International Conference on Learning Representations (ICLR) – Workshop on Physics for Machine Learning*, 2023. URL https://arxiv.org/abs/2303.04594.

Zi Hao Foo, Danyal Rehman, Orisa Z. Coombs, Akshay Deshmukh, and John H. Lienhard. Multicomponent Fickian solution-diffusion model for osmotic transport through membranes. *Journal of Membrane Science*, 640:119819, 2021. URL https://doi.org/10.1016/j.memsci.2021.119819.

Gretchen M. Mavrovouniotis and Howard Brenner. Hindered sedimentation, diffusion, and dispersion coefficients for brownian spheres in circular cylindrical pores. *Journal of Colloid and Interface Science*, 124(1):269–283, 1988. URL https://doi.org/10.1016/0021-9797(88)90348-7.

Jonathan Ennis, Heyou Zhang, Geoff W. Stevens, Jilska M. Perera, Peter J. Scales, and Steven L. Carnie. Mobility of protein through a porous membrane. *Journal of Membrane Science*, 119(1):47–58, 1996. URL https://doi.org/10.1016/0376-7388(96)00112-3.

Vítor Geraldes and Maria Diná Afonso. Prediction of the concentration polarization in the nanofiltration/reverse osmosis of dilute multi-ionic solutions. *Journal of Membrane Science*, 300(1):20–27, 2007. URL https://doi.org/10.1016/j.memsci.2007.04.025.

Yuefei Song, Qihua Hu, Tiemei Li, Yueke Sun, Xinxin Chen, and Jing Fan. Fabrication and characterization of phosphorylated chitosan nanofiltration membranes with tunable surface charges and improved selectivities. *Chemical Engineering Journal*, 352:163–172, 2018. URL https://doi.org/10.1016/j.cej.2018.07.010.

Omar Labban, Chang Liu, Tzyy Haur Chong, and John H. Lienhard. Fundamentals of low-pressure nanofiltration: Membrane characterization, modeling, and understanding the multi-ionic interactions in water softening. *Journal of Membrane Science*, 521:18–32, 2017. URL https://doi.org/10.1016/j.memsci.2016.08.062.

Yvana D. Ahdab, Danyal Rehman, and John H. Lienhard. Brackish water desalination for greenhouses: Improving groundwater quality for irrigation using monovalent selective electrodialysis reversal. *Journal of Membrane Science*, 610:118072, 2020. URL https://doi.org/10.1016/j.memsci.2020.118072.

Stefanie Postel, Carina Schneider, and Matthias Wessling. Solvent dependent solute solubility governs retention in silicone based organic solvent nanofiltration. *Journal of Membrane Science*, 497:47–54, 2016. URL https://doi.org/10.1016/j.memsci.2015.09.014.

J. Calvin Giddings, Eugene Kucera, Christopher Penn Russell, and Marcus N. Myers. Statistical theory for the equilibrium distribution of rigid molecules in inert porous networks. exclusion chromatography. *The Journal of Physical Chemistry*, 72(13):4397–4408, 1968. URL https://doi.org/10.1021/j100859a008.

Ken A. Dill and Sarina Bromberg. *Molecular Driving Forces: Statistical Thermodynamics in Biology, Chemistry, Physics, and Nanoscience*. Garland Science, 2011. ISBN 9780815344308.

Frederick G. Donnan. Theory of membrane equilibria and membrane potentials in the presence of non-dialysing electrolytes. a contribution to physical-chemical physiology. *Journal of Membrane Science*, 100(1):45–55, 1995. URL https://doi.org/10.1016/0376-7388(94)00297-C.

Yunjie Zhu, Haochen Zhu, Guangming Li, Zhaohuan Mai, and Yuliang Gu. The effect of dielectric exclusion on the rejection performance of inhomogeneously charged polyamide nanofiltration membranes. *Journal of Nanoparticle Research*, 21(10):1–13, 2019a. URL https://doi.org/10.1007/s11051-019-4665-4.

Danyal Rehman, Yvana D. Ahdab, and John H. Lienhard. Monovalent selective electrodialysis: Modelling multi-ionic transport across selective membranes. *Water Research*, 199:117171, 2021. URL https://doi.org/10.1016/j.watres.2021.117171.

Endre Nagy, Imre Hegedüs, Danyal Rehman, Quantum J. Wei, Yvana D. Ahdab, and John H. Lienhard. The need for accurate osmotic pressure and mass transfer resistances in modeling osmotically driven membrane processes. *Membranes*, 11(2), 2021. URL https://doi.org/10.3390/membranes11020128.

Kenneth S. Pitzer. Thermodynamics of electrolytes. I. Theoretical basis and general equations. *The Journal of Physical Chemistry*, 77(2):268–277, 1973. URL https://doi.org/10.1021/j100621a026.

Karan H. Mistry, Harrison A. Hunter, and John H. Lienhard. Effect of composition and nonideal solution behavior on desalination calculations for mixed electrolyte solutions with comparison to seawater. *Desalination*, 318:34–47, 2013. URL https://doi.org/10.1016/j.desal.2013.03.015.

Steven C. Chapra and Raymond Canale. *Numerical Methods for Engineers: With Software and Programming Applications*. McGraw-Hill Higher Education, 4th edition, 2001. ISBN 0072431938.

Arthur P. Dempster, Nam M. Laird, and Donald B. Rubin. Maximum likelihood from incomplete data via the em algorithm. *Journal of the Royal Statistical Society: Series B (Methodological)*, 39(1):1–22, 1977. URL https://doi.org/10.1111/j.2517-6161.1977.tb01600.x.

John H. Gaddum. Lognormal distributions. *Nature*, 156(3964):463–466, 1945. URL https://doi.org/10.1038/156463a0.

Bhaumik Sutariya and Santanu Karan. A realistic approach for determining the pore size distribution of nanofiltration membranes. *Separation and Purification Technology*, 293:121096, 2022. URL https://doi.org/10.1016/j.seppur.2022.121096.

Marina Micari, Dionysia Diamantidou, Sebastiaan G.J. Heijman, Massimo Moser, Amir Haidari, Henri Spanjers, and Valentin Bertsch. Experimental

and theoretical characterization of commercial nanofiltration membranes for the treatment of ion exchange spent regenerant. *Journal of Membrane Science*, 606:118117, 2020. URL https://doi.org/10.1016/j.memsci.2020.118117.

Gerrald Bargeman, Joannes B. Westerink, Olivia Guerra Miguez, and Matthias Wessling. The effect of nacl and glucose concentration on retentions for nanofiltration membranes processing concentrated solutions. *Separation and Purification Technology*, 134:46–57, 2014. URL https://doi.org/10.1016/j.seppur.2014.07.025.

Fan-Xin Kong, Hong-Wei Yang, Xiao-Mao Wang, and Yuefeng F. Xie. Assessment of the hindered transport model in predicting the rejection of trace organic compounds by nanofiltration. *Journal of Membrane Science*, 498:57–66, 2016. URL https://doi.org/10.1016/j.memsci.2015.09.062.

Andrea J.C. Semião, Matthieu Foucher, and Andrea I. Schäfer. Removal of adsorbing estrogenic micropollutants by nanofiltration membranes: Part b—modeldevelopment. *Journal of Membrane Science*, 431:257–266, 2013. URL https://doi.org/10.1016/j.memsci.2012.11.079.

Yagnaseni Roy, Mostafa H. Sharqawy, and John H. Lienhard. Modeling of flat-sheet and spiral-wound nanofiltration configurations and its application in seawater nanofiltration. *Journal of Membrane Science*, 493:360–372, 2015. URL https://doi.org/10.1016/j.memsci.2015.06.030.

Omar Labban, Chang Liu, Tzyy Haur Chong, and John H. Lienhard. Relating transport modeling to nanofiltration membrane fabrication: Navigating the permeability-selectivity trade-off in desalination pretreatment. *Journal of Membrane Science*, 554:26–38, 2018a. URL https://doi.org/10.1016/j.memsci.2018.02.053.

Wei Cheng, Caihong Liu, Tiezheng Tong, Razi Epsztein, Meng Sun, Rafael Verduzco, Jun Ma, and Menachem Elimelech. Selective removal of divalent cations by polyelectrolyte multilayer nanofiltration membrane: Role of polyelectrolyte charge, ion size, and ionic strength. *Journal of Membrane Science*, 559:98–106, 2018. URL https://doi.org/10.1016/j.memsci.2018.04.052.

Manas Ranjan Puhan, Bhaumik Sutariya, and Santanu Karan. Revisiting the alkali hydrolysis of polyamide nanofiltration membranes. *Journal of Membrane Science*, 661:120887, 2022. URL https://doi.org/10.1016/j.memsci.2022.120887.

Long D. Nghiem and Simon Hawkes. Effects of membrane fouling on the nanofiltration of pharmaceutically active compounds (phacs): Mechanisms and role of membrane pore size. *Separation and Purification Technology*, 57(1):176–184, 2007. URL https://doi.org/10.1016/j.seppur.2007.04.002.

Zi Hao Foo, Danyal Rehman, Andrew T. Bouma, Sebastien Monsalvo, and John H. Lienhard. Lithium concentration from salt-lake brine by Donnan-enhanced nanofiltration. *Environmental Science & Technology*, 2023. URL https://doi.org/10.1021/acs.est.2c08584.

Mayur Dalwani, Nieck E. Benes, Gerrald Bargeman, Dimitris Stamatialis, and Matthias Wessling. Effect of ph on the performance of polyamide/polyacrylonitrile based thin film composite membranes. *Journal of Membrane Science*, 372(1):228–238, 2011. URL https://doi.org/10.1016/j.memsci.2011.02.012.

Krešimir Košutić, Lidija Furač, László Sipos, and Branko Kunst. Removal of arsenic and pesticides from drinking water by nanofiltration membranes. *Separation and Purification Technology*, 42(2):137–144, 2005. URL https://doi.org/10.1016/j.seppur.2004.07.003.

Andriy E. Yaroshchuk. Negative rejection of ions in pressure-driven membrane processes. *Advances in Colloid and Interface Science*, 139(1):150–173, 2008. URL https://doi.org/10.1016/j.cis.2008.01.004. Membrane Electrochemistry: Selected papers from the 33rd Conference on Membrane Electrochemistry, Russia, May 2007.

Paloma Ortiz-Albo, Raquel Ibañez, Ane Urtiaga, and Inmaculada Ortiz. Phenomenological prediction of desalination brines nanofiltration through the indirect determination of zeta potential. *Separation and Purification Technology*, 210:746–753, 2019. URL https://doi.org/10.1016/j.seppur.2018.08.066.

Luis Pino-Soto, Alex Schwarz, Catalina Vargas, Florencia Saravia, Harald Horn, and Rodrigo Bórquez. Influence of multivalent-electrolyte metal solutions on the superficial properties and performance of a polyamide nanofiltration membrane. *Separation and Purification Technology*, 272:118846, 2021. URL https://doi.org/10.1016/j.seppur.2021.118846.

Yagnaseni Roy, David M. Warsinger, and John H. Lienhard. Effect of temperature on ion transport in nanofiltration membranes: Diffusion, convection and electromigration. *Desalination*, 420:241–257, 2017. URL https://doi.org/10.1016/j.desal.2017.07.020.

Yagnaseni Roy and John H. Lienhard. Factors contributing to the change in permeate quality upon temperature variation in nanofiltration. *Desalination*, 455:58–70, 2019. URL https://doi.org/10.1016/j.desal.2018.12.017.

Paz Nativ, Olga Leifman, Ori Lahav, and Razi Epsztein. Desalinated brackish water with improved mineral composition using monovalent-selective nanofiltration followed by reverse osmosis. *Desalination*, 520:115364, 2021. URL https://doi.org/10.1016/j.desal.2021.115364.

Omar Labban, Tzyy Haur Chong, and John H. Lienhard. Design and modeling of novel low-pressure nanofiltration hollow fiber modules for water softening and desalination pretreatment. *Desalination*, 439:58–72, 2018b. URL https://doi.org/10.1016/j.desal.2018.04.002.

Jacqueline L. Stair, Jeremy J. Harris, and Merlin L. Bruening. Enhancement of the ion-transport selectivity of layered polyelectrolyte membranes through cross-linking and hybridization. *Chemistry of Materials*, 13(8):2641–2648, 2001. URL https://doi.org/10.1021/cm010166e.

Yufan Hao, Na Yang, Longfei Zhang, Yao Fang, Yongli Sun, Bin Jiang, and Luhong Zhang. Tailored design of highly permeable polyamide-based nanofiltration membrane via a complex-dissociation regulated interfacial polymerization. *Chemical Engineering Journal*, 452:139197, 2023. URL https://doi.org/10.1016/j.cej.2022.139197.

Zhuyuan Wang, Songmiao Liang, Yuan Kang, Wang Zhao, Yun Xia, Jindi Yang, Huanting Wang, and Xiwang Zhang. Manipulating interfacial polymerization for polymeric nanofilms of composite separation membranes. *Progress in Polymer Science*, 122:101450, 2021a. URL https://doi.org/10.1016/j.progpolymsci.2021.101450.

Abdul Latif Ahmad and Boon Seng Ooi. A study on acid reclamation and copper recovery using low pressure nanofiltration membrane. *Chemical Engineering Journal*, 156(2):257–263, 2010. URL https://doi.org/10.1016/j.cej.2009.10.014.

Cody L. Ritt, J. Pedro de Souza, Michelle G. Barsukov, Shari Yosinski, Martin Z. Bazant, Mark A. Reed, and Menachem Elimelech. Thermodynamics of charge regulation during ion transport through silica nanochannels. *ACS Nano*, 16(9):15249–15260, 2022. URL https://doi.org/10.1021/acsnano.2c06633.

Vladislav Pavluchkov, Idit Shefer, Ophir Peer-Haim, Jens Blotevogel, and Razi Epsztein. Indications of ion dehydration in diffusion-only and pressure-driven nanofiltration. *Journal of Membrane Science*, 648:120358, 2022. URL https://doi.org/10.1016/j.memsci.2022.120358.

Xiaohu Zhai, Yong-Lei Wang, Ruobin Dai, Xuesong Li, and Zhiwei Wang. Roles of anion–cation coupling transport and dehydration-induced ion–membrane interaction in precise separation of ions by nanofiltration membranes. *Environmental Science & Technology*, 56(19):14069–14079, 2022. URL https://doi.org/10.1021/acs.est.2c04772.

Razi Epsztein, Evyatar Shaulsky, Nadir Dizge, David M. Warsinger, and Menachem Elimelech. Role of ionic charge density in donnan exclusion of monovalent anions by nanofiltration. *Environmental Science & Technology*, 52(7):4108–4116, 2018. URL https://doi.org/10.1021/acs.est.7b06400.

Zhi-yong Wang and Yu-qiang Ma. A molecular simulation study on the role of ion sizes and dielectric images in near-surface ion distribution far from the strong coupling limit. *The Journal of Chemical Physics*, 136(23):234701, 2012. URL https://doi.org/10.1063/1.4729311.

Yunjie Zhu, Haochen Zhu, Guangming Li, Zhaohuan Mai, and Yuliang Gu. The effect of dielectric exclusion on the rejection performance of inhomogeneously charged polyamide nanofiltration membranes. *Journal of Nanoparticle Research*, 21(10):217, 2019b. doi: 10.1007/s11051-019-4665-4. URL https://doi.org/10.1007/s11051-019-4665-4.

Farzad Fadaei, Vahid Hoshyargar, Saeed Shirazian, and Seyed Nezameddin Ashrafizadeh. Mass transfer simulation of ion separation by nanofiltration considering electrical and dielectrical effects. *Desalination*, 284:316–323, 2012. URL https://doi.org/10.1016/j.desal.2011.09.018.

Andriy E. Yaroshchuk, Merlin L. Bruening, and Emiliy Zholkovskiy. Modelling nanofiltration of electrolyte solutions. *Advances in Colloid and Interface Science*, 268:39–63, 2019. URL https://doi.org/10.1016/j.cis.2019.03.004.

Robert A Robinson and Robert H Stokes. *Electrolyte solutions*. Dover Publications, Mineola, New York, 2nd edition, 2002. ISBN 0486422259.

Abderrahim Dinane, Mohamed El Guendouzi, and Abdelfetah Mounir. Hygro-

metric determination of water activities, osmotic and activity coefficients of (NaCl+ KCl)(aq) at T=298.15 K. *The Journal of Chemical Thermodynamics*, 34(4):423–441, 2002. URL https://doi.org/10.1006/jcht.2001.0845.

Donald G. Archer and Peiming Wang. The dielectric constant of water and debye-hückel limiting law slopes. *Journal of Physical and Chemical Reference Data*, 19(2):371–411, 1990. URL https://doi.org/10.1063/1.555853.

Kishor G. Nayar, Mostafa H. Sharqawy, Leonardo D. Banchik, and John H. Lienhard V. Thermophysical properties of seawater: A review and new correlations that include pressure dependence. *Desalination*, 390:1–24, 2016. URL https://doi.org/10.1016/j.desal.2016.02.024.

Johan Schaep, Carlo Vandecasteele, Abdul Wahab Mohammad, and W. Richard Bowen. Analysis of the salt retention of nanofiltration membranes using the donnan–steric partitioning pore model. *Separation Science and Technology*, 34(15):3009–3030, 1999. URL https://doi.org/10.1081/SS-100100819.

Li Wang, Danyal Rehman, Peng-Fei Sun, Akshay Deshmukh, Liyuan Zhang, Qi Han, Zhe Yang, Zhongying Wang, Hee-Deung Park, John H. Lienhard, and Chuyang Y. Tang. Novel positively charged metal-coordinated nanofiltration membrane for lithium recovery. *ACS Applied Materials & Interfaces*, 13(14):16906–16915, 2021b. URL https://doi.org/10.1021/acsami.1c02252.

Sheehan Olver and Alex Townsend. A fast and well-conditioned spectral method. *SIAM Review*, 55(3):462–489, 2013. URL https://doi.org/10.1137/120865458.

Lloyd N. Trefethen. *Spectral Methods in MATLAB*. Software, Environments, and Tools. Society for Industrial and Applied Mathematics (SIAM, 3600 Market Street, Floor 6, Philadelphia, PA 19104), 2000. ISBN 9780898719598.